Weakly nonlinear broadband and multi-directional surface waves on an arbitrary depth: A framework, Stokes drift, and particle trajectories

Yan Li (李艳)**, and Xin Li** (李欣)

View Online   Export Citation   CrossMark

ARTICLES YOU MAY BE INTERESTED IN

Physics of Fluids
SPECIAL TOPIC: Flow and Acoustics of Unmanned Vehicles
Submit Today!

Weakly nonlinear broadband and multi-directional surface waves on an arbitrary depth: A framework, Stokes drift, and particle trajectories

View Online　　Export Citation　　CrossMark

Yan Li (李艳),[1,2,a] (iD) and Xin Li (李欣)[3,b]

AFFILIATIONS

[1] Department of Energy and Process Engineering, Norwegian University of Science and Technology, N-7491 Trondheim, Norway
[2] Department of Engineering Science, University of Oxford, Parks Road, Oxford OX1 3PJ, United Kingdom
[3] State Key Laboratory of Ocean Engineering, School of Naval Architecture, Ocean and Civil Engineering, Shanghai Jiao Tong University, Shanghai 200240, China

[a] Author to whom correspondence should be addressed: yan.li@ntnu.no
[b] Electronic mail: lixin@sjtu.edu.cn

ABSTRACT

Surface gravity waves in coastal waters are broadband and multi-directional, whose quadratic properties are of considerable engineering and scientific interest. Based on a Stokes expansion and an envelope-type framework, a new semi-analytical approach is proposed in this paper for the description of weakly nonlinear broadband and multi-directional surface waves. This approach proposes solving for the second-order wave fields through the separation of harmonics, by using a Fast Fourier transform and a time integration method. Different from some other methods, e.g., the High-Order Spectral method, the approach introduces a spectral shift for the superharmonic waves, leading to computationally efficient and accurate spectral predictions. The approach has been validated through comparisons with the results based on Dalzell ["A note on finite depth second-order wave–wave interactions," Appl. Ocean Res. **21**, 105–111 (1999)]. An envelope-type framework for the fast prediction of particle trajectories and Stokes drifts up to the second order in wave steepness is also derived in this paper, based on the semi-analytical approach. This paper shows that the results based on a narrowband assumption lead to underestimates of Stokes drift velocities driven by broadband unidirectional focused wave groups. The cases, examined for particle trajectories below broadband unidirectional focused wave groups, show that a larger bandwidth and water depth can enhance the differences in the net mean horizontal displacement of particles at water surface relative to these at seabed.

I. INTRODUCTION

Surface gravity waves in the open ocean and coastal regions interact with their ambient environment, e.g., varying bathymetries, currents, turbulence, and wind actions, and are essential to energy and momentum transfers and vertical mixing in the upper ocean. They lead to extreme forces and contribute to fatigue loads on offshore structures under different sea states. Therefore, good understanding of wave properties can contribute to a range of subjects, such as fluid dynamics and hydrodynamics.

Wave properties have been extensively investigated in experimental, numerical, and theoretical studies; a majority of which have focused on long-crested waves on water of different depths. For waves on a finite depth, wave properties are affected by a seabed in various manners, such as altering the dispersion relation[1,2] and wave amplitude,[3]

and triggering wave breaking.[4–6] In recent years, an enhanced occurrence probability of extremely large wave events has been attributed to depth transitions.[6–11] This paper focuses on weakly nonlinear waves on waters of an intermediate uniform depth, i.e., for $0.5 \lesssim kh$ and $kh \sim \mathcal{O}(1)$ where k and h are the characteristic wavenumber and water depth, respectively.

A second-order expansion of wave fields in wave steepness can capture the effects of weak nonlinearity and has been demonstrated to work effectively in the last decades. For the description of monochromatic waves, the Stokes second-order theory has been well understood on an arbitrary constant depth.[12] Forcing of the second-order superharmonic wave leads to an increase in wave crest and a decrease in wave trough without a change in the wave height.[13] For irregular waves, second-order effects lead to the

forcing of superharmonic and subharmonic waves, which do not obey the linear dispersion relation and, therefore, are bound to the linear free contents (see, e.g., Phillips[14] and Longuet-Higgins[15]). These second-order waves can lead to expanding the linear wave energy spectrum and are also responsible for the quadratic forces on offshore structures, which are important for the fatigue and extreme wave loads (see, e.g., Newman,[16] Molin,[17] and Grue[18]).

For examining the properties of second-order waves and their roles for different purposes, theoretical approaches have been proposed for the description of second-order irregular waves. Table I shows a summary of these theoretical works in different regimes of applicability, in addition to the well-known Stokes second-order theory for monochromatic waves,[29] waves in shallow water, and the Boussinesq-type approximations (see, e.g., Wei et al.[30]). The theory for the interaction of two waves is presented by Longuet-Higgins[15] for deep water and by Hasselmann,[26] Sharma and Dean,[27] and Dalzell[28] for a finite depth. This permits the analysis of weakly nonlinear irregular waves of an arbitrary bandwidth, i.e., the so-called broadband wave theory.[31] With leading order approximations to the linear dispersion relation under the so-called narrowband assumption, the slow modulation of Stokes waves can be investigated with second-order wave fields being expressed in an envelope-type form.[3,19,20,25,32–34] The narrowband approximation to the description of second-order waves has been widely used in wave modeling based on high-order nonlinear Schrödinger equations (NLSEs) for the spatial and temporal modulations of the wave envelope of linear surface elevation.[35] Comparing alternative numerical methods like the High-Order Spectral (HOS) method (see, e.g., Dommermuth and Yue[36] and West et al.[37]), a key feature of the NLSE-based models is its low computational cost as it allows for the computational parameters chosen according to the scaling of the wave envelope (see, e.g., Lo and Mei[38]) and, hence, it demands a much smaller number of the discrete points in the computational domain. Second-order statistical models for the statistical properties of irregular random waves are developed,[39–41] and the roles of water depth on the statistical properties are examined in papers, e.g., Tang and Adcock,[42] Myrhaug,[43] Myrhaug et al.,[44] and references therein.

In recent years, attempts have been made into accounting for the interaction of surface waves with ambient environments, e.g., coastal bathymetries, currents, turbulence, and wind actions, which often requires a fast and accurate prediction of the spatial and temporal evolution of the three-dimensional fields driven by broadband directional spread surface waves. This makes the aforementioned broadband theory (e.g., Dalzell[28]) a less favored candidate due to its relatively low efficiency in computations. The same reason prohibits using numerical solvers (cf., e.g., Zheng et al.,[8] Engsig-Karup et al.,[45] and Bihs et al.[46]), which apply direct numerical solutions of the fully nonlinear potential flow equations and which have been increasingly used in recent years. The prediction of waves of a broad bandwidth is obviously beyond the regime of applicability of the NLSE-based models due to the narrowband assumption.[20,25,33] Therefore, the development of the novel theory that can offer accurate and computationally efficient prediction would be beneficial. To this end, the first objective of this paper is to propose a novel semi-analytical approach where low-order wave fields are expressed in an envelope-type form. Specifically, this method shares the same advantage as the narrowband NLSE-based models in terms of the computational efficiency. It can also permit a straightforward generalization to a high-order NLS equation that contributes to relax the narrowband assumption used in previous papers (e.g., Davey and Stewartson[20] and Slunyaev[25]). This will be addressed in future work.

A noticeable quadratic property of linear surface waves is the Stokes drift, which is widely known.[29] It is essential for transporting fluid particles in the upper ocean and driving Langmuir circulations.[47–50] Approximations to the vertical profile of Stokes drift underneath broadband surface waves on deep water have been proposed based on the results for monochromatic waves.[51,52] Webb and Fox-Kemper[53] examined the impact of wave directionality on estimating Stokes drift. Lagrangian paths of particles driven by steep monochromatic and irregular waves on a finite depth are experimentally examined by Grue and Kolass[54] and Grue and Jensen,[55] respectively. Below short wave groups (or wave packets), the net Lagrangian displacement of fluid particles is driven primarily by Stokes drift velocity and the second-order Eulerian return flows.[47,56] With a narrowband

TABLE I. A summary of the theoretical frameworks of different regimes of applicability for the prediction of second-order irregular waves with $0.5 \lesssim kh$, where k denotes the characteristic wavenumber and h is the water depth, in addition to the Boussinesq-type equations. In the table, N denotes the total number of the discrete points (or Fourier modes) chosen in the computational domain and δ denotes the dimensionless bandwidth of a wave spectrum.

	Bandwidth (δ)	Depth regime	Computational complexity	Order of accuracy
Dysthe[19]	Narrowband	Deep ($\pi \lesssim kh$)	$\mathcal{O}(N\ln N)$	Up to $\mathcal{O}(\delta)$
Davey and Stewartson[20] Trulsen et al.[21] Gramstad[22] and Calvert et al.[23]	Narrowband	Arbitrary ($0.5 \lesssim kh$)	$\mathcal{O}(N\ln N)$	Up to $\mathcal{O}(\delta)$
Brinch-Nielsen and Jonsson[24] Slunyaev[25]	Narrowband	Arbitrary	$\mathcal{O}(N\ln N)$	Up to $\mathcal{O}(\delta^2)$
Longuet-Higgins[15]	Arbitrary	Deep	$\mathcal{O}(N^2)$	Arbitrary order in δ
Hasselmann[26] Sharma and Dean[27] Dalzell[28]	Arbitrary	Arbitrary	$\mathcal{O}(N^2)$	Arbitrary order in δ
This paper	Arbitrary	Arbitrary	$\mathcal{O}(N\ln N)$	Arbitrary order in δ

wave assumption, the particle trajectories below wave packets have been examined analytically on finite depth[57] and measured experimentally on deep water[58] and finite water.[23]

To the authors' knowledge, studies on the particle trajectories and Stokes drift profiles below a broadband short wave group on a finite depth are scarce. This is likely due to challenges in the studies based on the measurements in both a numerical and laboratory wave tank, as explained in the following. The wave generation by a wavemaker can lead to spurious waves, which would trigger additional physics, posing big challenges in the post-processing of data (see, e.g., Schäffer[59] and Paprota[60]). The limited length of a wave tank may be another source of challenge since it may lead to a rapid reflection of the second-order subharmonic contents from the end of a tank, which, as a result, significantly affects the mean flow fields driven by waves on a finite depth, as reflected in a number of papers, e.g., Calvert et al.,[23] Paprota,[60] and Li et al.[61] This paper intends to fill in this gap through deriving a framework for the particle trajectories below broadband surface waves, which can simply conquer these aforementioned challenges. Specifically, the roles of water depth, bandwidth, and spatial evolution of wave groups in the net mean horizontal displacements and trajectories of particles and Stokes drift velocity are assessed in this paper.

The paper is laid out as follows. The problem definition and linear wave fields are presented in Sec. II. A novel semi-analytical approach for the second-order broadband waves on an intermediate water depth is derived in Sec. III. This approach proposes solving for the second-order wave fields through the separation of harmonics, by using a Fast Fourier transform (FFT) and a time integration method. Based on the semi-analytical approach, the description of the trajectories of fluid particles and Stokes drift profile is presented in Sec. IV. The results are shown in Sec. V where the validations of the new approach through comparisons with the exact approach by Dalzell[28] are given and the roles of water depth, spatial evolution of a short focused wave group, and the wave bandwidth in Stokes drift and particle trajectories are examined. Conclusions of this paper are drawn in Sec. VI.

II. MATHEMATICAL FORMULATION
A. Problem definition

We consider ocean surface waves propagating in water of a finite constant depth in the framework of potential-flow theory, assuming incompressible inviscid flows, irrotational fluid motions, and negligible effects of surface tension. A Cartesian coordinate system is chosen with the undisturbed water surface located at $z = 0$. The system of surface waves on a finite depth can be described as a boundary value problem governed by the Laplace equation

$$\nabla_3^2 \Phi = 0 \quad \text{for} \quad -h < z < \zeta(\mathbf{x}, t), \tag{1}$$

where $\Phi(\mathbf{x}, z, t)$ denotes the velocity potential, $\zeta(\mathbf{x}, t)$ is the free surface elevation, $\mathbf{x}$ is the position vector in the horizontal plane, t is the time, h denotes the constant water depth, and $\nabla_3 = (\nabla, \partial_z)$ with $\nabla = (\partial_x, \partial_y)$ is the gradient in the horizontal plane. Equation (1) should be solved subject to the nonlinear kinematic and combined boundary conditions (see, e.g., Davey and Stewartson[20]) at the free water surface $z = \zeta(\mathbf{x}, t)$,

$$\partial_t \zeta + \nabla \Phi \cdot \nabla \zeta - \partial_z \Phi = 0$$
$$\Gamma \Phi + \partial_t (\nabla_3 \Phi)^2 + \frac{1}{2} \nabla_3 \Phi \cdot \nabla_3 (\nabla_3 \Phi)^2 = 0, \tag{2}$$

where the operator Γ is defined as $\Gamma = \partial_{tt} + g\partial_z$ with g the gravitational acceleration; a seabed boundary condition

$$\partial_z \Phi = 0 \quad \text{for} \quad z = -h. \tag{3}$$

B. Stokes expansion and separation of harmonics

In order to solve the boundary value problem (1)–(3), we seek the solutions of unknowns Φ and ζ in a form of power series in wave steepness $\epsilon = kA_0$ (a so-called Stokes expansion), with the characteristic wavenumber k and wave amplitude A_0, respectively,

$$\Phi = \epsilon \Phi^{(1)} + \epsilon^2 \Phi^{(2)} + \mathcal{O}(\epsilon^3) \tag{4a}$$

$$\zeta = \epsilon \zeta^{(1)} + \epsilon^2 \zeta^{(2)} + \mathcal{O}(\epsilon^3), \tag{4b}$$

where we consider up to the second order and the superscripts denote the order in ϵ. Substituting (4a) and (4b) into the boundary value problem (1)–(3) leads to the decomposition of the fully nonlinear system into different problems through a collection of the terms at the same order in ϵ. The decomposed problems can be solved successively from the lowest to higher orders, as presented in Secs. II C and III. For later reference, we define an inverse Fourier transform with respect to $\mathbf{k}$ for an arbitrary field $\chi(\mathbf{x})$ as follows:

$$\chi(\mathbf{x}) = \int_{-\infty}^{\infty} \hat{\chi}(\mathbf{k}) e^{i\mathbf{k} \cdot \mathbf{x}} d\mathbf{k}, \tag{5}$$

where $\hat{\chi}$ denotes the expression for the arbitrary parameter χ in the Fourier $\mathbf{k}$ space. Following Trulsen et al.,[62] linear surface elevation $\zeta^{(1)}$ is expressed in two different but equating forms as follows:

$$\zeta^{(1)}(\mathbf{x}, t) = \frac{1}{2} A(\mathbf{x}, t) e^{i(\mathbf{k}_0 \cdot \mathbf{x} - \omega_0 t)} + \text{c.c.}, \tag{6a}$$

or

$$\zeta^{(1)}(\mathbf{x}, t) = \frac{1}{2} \int_{-\infty}^{\infty} \hat{\zeta}^{(1)}(\mathbf{k}, t) e^{i\mathbf{k} \cdot \mathbf{x}} d\mathbf{k} + \text{c.c.} \tag{6b}$$
$$\text{with} \quad \hat{\zeta}(\mathbf{k}, t_0) = \hat{\zeta}(\mathbf{k}, t_0) e^{-i\omega(\mathbf{k})(t - t_0)},$$

in which c.c. denotes the complex conjugates, t_0 denotes an initial instant, A denotes the linear (complex) wave envelope of the carrier wave of vector $\mathbf{k}_0 = (k_0, 0)$ chosen along the x direction in the horizontal plane, ω_0 denotes the angular frequency of the carrier wave that is obtained from the linear dispersion relation $\omega_0 = \omega(\mathbf{k}_0)$ with $\omega(\mathbf{k}) = \sqrt{gk \tanh kh}$, where $\mathbf{k} = (k_x, k_y)$ $(k = |\mathbf{k}|)$ denotes a wave vector in the horizontal plane. Equation (6a) for $\zeta^{(1)}$ denotes an envelope-type form, and Eq. (6b) denotes a form through the linear superposition of monochromatic waves in the Fourier $\mathbf{k}$ plane. This paper focuses on the former and derives second-order solutions based on it for both Φ and ζ. This would permit straightforward extension to higher order problems that are based on harmonic expansions, such as

a third-order nonlinear Schrödinger equation for the envelope of the elevation of the first-harmonic, A.

Equating (6a) and (6b), we obtain an explicit expression for linear envelope $[A(\mathbf{x}, t)]$ that is valid for waves of an arbitrary bandwidth as follows:

$$A(\mathbf{x}, t) = \int_{-\infty}^{\infty} \hat{A}(\mathbf{k}, t) e^{i\mathbf{k}\cdot\mathbf{x}} d\mathbf{k} \quad (7a)$$

with

$$\hat{A}(\mathbf{k}, t) = \hat{A}(\mathbf{k}, t_0) e^{-i[\omega(\mathbf{k}+\mathbf{k}_0)-\omega_0](t-t_0)}$$
$$\hat{A}(\mathbf{k}, t_0) = \hat{\zeta}(\mathbf{k} + \mathbf{k}_0, t_0) e^{i\omega_0 t_0}, \quad (7b)$$

where the integral variable was first replaced with $\mathbf{k}' = \mathbf{k} - \mathbf{k}_0$ and the prime was subsequently removed. Using an envelope-type form similar to (6a), ζ and Φ can be expressed in a form of harmonic expansions as follows:

$$\Phi(\mathbf{x}, z, t) = \left[\frac{1}{2}\epsilon B(\mathbf{x}, z, t) e^{i(\mathbf{k}_0\cdot\mathbf{x}-\omega_0 t)} + \text{c.c.}\right] + \epsilon^2 \Phi^{(20)}(\mathbf{x}, z, t)$$
$$+ \epsilon^2 \left[\Phi^{(22)}(\mathbf{x}, z, t) + \text{c.c.}\right] + \mathcal{O}(\epsilon^3), \quad (8a)$$

$$\zeta(\mathbf{x}, t) = \left[\frac{1}{2}\epsilon A e^{i(\mathbf{k}_0\cdot\mathbf{x}-\omega_0 t)} + \text{c.c.}\right] + \epsilon^2 \zeta^{(20)}$$
$$+ \epsilon^2 \left[\zeta^{(22)} + \text{c.c.}\right] + \mathcal{O}(\epsilon^3), \quad (8b)$$

in which superscripts "(ij)" denote $\mathcal{O}(\epsilon^i)$ and j-th harmonic and B denotes the linear (complex) envelope of the carrier wave potential. For later reference in Sec. III, we express the second-order superharmonic component of ζ and Φ in a form as follows, respectively:

$$\zeta^{(22)}(\mathbf{x}, t) = \frac{1}{2}A^{(22)}(\mathbf{x}, t) e^{2i(\mathbf{k}_0\cdot\mathbf{x}-\omega_0 t)} \quad (9a)$$

and

$$\Phi^{(22)}(\mathbf{x}, z, t) = \frac{1}{2}B^{(22)}(\mathbf{x}, z, t) e^{2i(\mathbf{k}_0\cdot\mathbf{x}-\omega_0 t)}, \quad (9b)$$

where $A^{(22)}(\mathbf{x}, t)$ and $B^{(22)}(\mathbf{x}, z, t)$ denote the envelope of the second-order superharmonic elevation and potential, respectively.

C. Linear velocity and potential

For convenience, we introduce the envelope-type expression for linear velocity $\mathbf{V}^{(1)}(\mathbf{x}, z, t) = [\mathbf{u}^{(1)}(\mathbf{x}, z, t), w^{(1)}(\mathbf{x}, z, t)]$, where $\mathbf{u}^{(1)}$ and $w^{(1)}$ denote the velocity in the horizontal plane and the vertical direction, respectively,

$$\mathbf{V}^{(1)}(\mathbf{x}, z, t) = \frac{1}{2}\bar{\mathbf{V}}(\mathbf{x}, z, t) e^{i(\mathbf{k}_0\cdot\mathbf{x}-\omega_0 t)} + \text{c.c.} \quad (10a)$$

with

$$\bar{\mathbf{V}} \equiv [\bar{\mathbf{u}}(\mathbf{x}, z, t), \bar{w}(\mathbf{x}, z, t)], \quad (10b)$$

where $\bar{\mathbf{V}}$ denotes the linear velocity envelope (vector) of carrier wave $\mathbf{k}_0$ without adding the superscript "(1)" for simplicity, whose components in the horizontal plane and vertical direction

are defined as $\bar{\mathbf{u}}$ and $\bar{w}$, respectively. The linearized boundary value problem (1)–(3) can be readily solved for the linear wave fields in the Fourier $\mathbf{k}$ plane. Without the detailed derivations (see, e.g., Sec. 13 in Mei *et al.*[63]), we obtain the expression for linear velocity envelope, $\bar{\mathbf{V}}$, and potential, B, in the Fourier $\mathbf{k}$ plane as a function of the linear envelope $[\hat{A}(\mathbf{k})]$ in the Fourier plane as follows:

$$\hat{B}(\mathbf{k}, z, t) = -i\frac{\omega(\mathbf{k}+\mathbf{k}_0)}{|\mathbf{k}+\mathbf{k}_0|}\frac{\cosh|\mathbf{k}+\mathbf{k}_0|(z+h)}{\sinh|\mathbf{k}+\mathbf{k}_0|h}\hat{A}(\mathbf{k}, t)e^{i\mathbf{k}\cdot\mathbf{x}}, \quad (11a)$$

$$\hat{\mathbf{u}}(\mathbf{k}, z, t) = \frac{(\mathbf{k}+\mathbf{k}_0)\omega(\mathbf{k}+\mathbf{k}_0)}{|\mathbf{k}+\mathbf{k}_0|}\frac{\cosh|\mathbf{k}+\mathbf{k}_0|(z+h)}{\sinh|\mathbf{k}+\mathbf{k}_0|h}\hat{A}(\mathbf{k}, t, t) \quad (11b)$$

and

$$\hat{w}(\mathbf{k}, z, t) = -i\hat{A}(\mathbf{k}, t)\omega(\mathbf{k}+\mathbf{k}_0)\frac{\sinh[|\mathbf{k}+\mathbf{k}_0|(z+h)]}{\sinh(|\mathbf{k}+\mathbf{k}_0|h)}, \quad (11c)$$

where $\hat{B}$, $\hat{\mathbf{u}}$, and $\hat{w}$ denote B, $\bar{\mathbf{u}}$, and $\bar{w}$ in the Fourier $\mathbf{k}$ plane, respectively. Therefore, with (11a), (11b), and (11c), if linear elevation $\zeta^{(1)}(\mathbf{x}, t)$ is given at an initial instant t_0, linear velocity envelope, $\bar{\mathbf{V}}(\mathbf{x}, z, t)$, and potential envelope, B, can be readily obtained from an inverse Fourier transform.

III. SECOND-ORDER SOLUTIONS

With linear solutions to the linearized boundary value problem (1)–(3) given in Sec. II, this section seeks the solutions for unknowns $\zeta^{(2)}$ and $\Phi^{(2)}$. The insertion of unknowns Φ and ζ described by (8a) and (8b), respectively, into the boundary value problem (1)–(3) and the collection of the terms at the second order in wave steepness leads to a boundary value problem for the second-order potential, $\Phi^{(2)}$, as follows:

$$\nabla_3^2 \Phi^{(2)} = 0 \quad \text{for} \quad -h < z < \zeta \quad (12a)$$

$$(\partial_{tt} + g\partial_z)\Phi^{(2)} = F^{(2)}(\mathbf{x}, z, t) \quad \text{for} \quad z = 0, \quad (12b)$$

$$\partial_z \Phi^{(2)} = 0 \quad \text{for} \quad z = -h, \quad (12c)$$

where $F^{(2)}$ denotes the forcing at the second order by linear waves, defined as

$$F^{(2)}(\mathbf{x}, z, t) = -\zeta^{(1)}\Gamma_z\Phi^{(1)} - \partial_t(\nabla_3\Phi^{(1)})^2 \quad \text{with} \quad \Gamma_z = \partial_z\Gamma. \quad (13)$$

Inserting the expression for the linear wave fields presented in Sec. II C into (13) leads to the forcing term, $F^{(2)}$, in a form of the superposition of two different wave harmonics as follows:

$$F^{(2)}(\mathbf{x}, z, t) = \left[F^{(22)}(\mathbf{x}, z, t)e^{2i(\mathbf{k}_0\cdot\mathbf{x}-\omega_0 t)} + \text{c.c.}\right] + F^{(20)}(\mathbf{x}, z, t), \quad (14a)$$

with

$$F^{(22)}(\mathbf{x}, z, t) = -\frac{1}{4}\left[A(\Gamma - 2i\omega_0\partial_t - \omega_0^2)\bar{w} + (\partial_t - 2i\omega_0)(\bar{\mathbf{V}}\cdot\bar{\mathbf{V}})\right], \quad (14b)$$

and

$$F^{(20)}(\mathbf{x}, z, t) = -\frac{1}{4}\left(A^*(\Gamma - 2\mathrm{i}\omega_0\partial_t - \omega_0^2)\bar{w} + \text{c.c.}\right) - \frac{1}{2}\partial_t(\bar{\mathbf{V}} \cdot \bar{\mathbf{V}}^*),$$

(14c)

where the asterisk denotes the complex conjugates, the superscripts "22" and "20" denote the superharmonic and subharmonic, respectively. Due to (14a), the solution to the boundary value problem (12) for the second-order potential, $\Phi^{(2)}$, can be expressed as the superposition of two independent parts: one for superharmonic potential, $\Phi^{(22)}$, and the other for subharmonic potential $\Phi^{(20)}$. Therefore, the boundary value problems for the two contents are described by

$$\nabla_3^2 \Phi^{(2j)} = 0 \quad \text{for} \quad -h < z < \zeta,$$

(15a)

$$(\partial_{tt} + g\partial_z)\Phi^{(2j)} = F^{(2j)}(\mathbf{x}, z, t)e^{2ji(\mathbf{k}_0 \cdot \mathbf{x} - \omega_0 t)} \quad \text{for} \quad z = 0$$

(15b)

$$\partial_z \Phi^{(2j)} = 0 \quad \text{for} \quad z = -h,$$

(15c)

where j denotes j-th harmonic with $j = 0$ and $j = 2$ for the second-order subharmonic $[\Phi^{(20)}]$ and superharmonic potential $[\Phi^{(22)}]$, respectively.

A. A novel semi-analytical approach

Using the linear wave fields presented in Secs. II B and II C, this section proposes solving the boundary value problem (15a), (15b), and (15c) for the second-order potentials $[\Phi^{(2j)}]$ by using a *semi-analytical approach*. *The semi-analytical approach* is composed of the following three consecutive steps for numerical implementations that are based on a pseudospectral method,[64] Fourier transform with respect to $\mathbf{x}$, and a numerical time integration method. Specifically, the first step is to evaluate the forcing term, $F^{(2)}$, on still water surface by using a pseudospectral method.[64] The next step is to seek an explicit structure for the second-order potentials [i.e., $\Phi^{(22)}$ and $\Phi^{(20)}$] with respect to z in the Fourier $\mathbf{k}$ space. The last step is to solve a second-order differential equation with respect to time with a time integration method. We explain separately the solution for superharmonic and subharmonic waves in Secs. III A 1 and III A 2.

1. Superharmonic waves

Following the procedures of the semi-analytical approach, we first apply a Fourier transform with respect to $\mathbf{x}$ for the terms on both sides of the boundary condition at still water surface described in (15) and obtain

$$\left[(\partial_t - 2\mathrm{i}\omega_0)^2 + g\partial_z\right]\hat{B}^{(22)}(\mathbf{k}, z, t) = 2\hat{F}^{(22)}(\mathbf{k}, z, t) \quad \text{for } z = 0,$$

(16)

where $\hat{F}^{(22)}$ denotes the Fourier transform for $F^{(22)}$ with respect to $\mathbf{x}$. Due to that the Laplace equation for the superharmonic potential $[\Phi^{(22)}]$, an explicit expression for the envelope of the superharmonic potential in the Fourier plane, $\hat{B}^{(22)}(\mathbf{k}, z, t)$, can be assumed in a form as follows:

$$\hat{B}^{(22)}(\mathbf{k}, z, t) = \hat{B}^{(22)}(\mathbf{k}, 0, t)\frac{\cosh|\mathbf{k} + 2\mathbf{k}_0|(z + h)}{\cosh|\mathbf{k} + 2\mathbf{k}_0|h}.$$

(17)

Inserting (17) into (16) leads to

$$\left[(\partial_t - 2\mathrm{i}\omega_0)^2 + g|\mathbf{k} + 2\mathbf{k}_0|\tanh|\mathbf{k} + 2\mathbf{k}_0|h\right]\hat{B}^{(22)}(\mathbf{k}, 0, t)$$
$$= 2\hat{F}^{(22)}(\mathbf{k}, 0, t).$$

(18)

The third step is to solve the second-order differential equation (18) for $\hat{B}^{(22)}(\mathbf{k}, 0, t)$ by numerical integration methods for the time derivatives, given that homogeneous solutions of (18) are not admitted for stationary waves [see, e.g., Phillips[14] and page 848, Eq. (14.3.4) in Mei et al.[63]]. For numerical implementations, additional initial conditions at an instant, t_0, are required. We remark here that multiple choices are available for different purposes of wave generation. For instance, a second-order wavemaker theory is based on Schäffer,[59] periodic boundary conditions as in Dommermuth and Yue,[36] the framework by Bonnefoy et al.[65] for the wave making in a numerical wave tank, and stationary waves based on Dalzell.[28] In this paper, we assume that initial conditions for second-order wave fields are given and we use the inputs based on Dalzell[28] for numerical implementations for the results presented in Sec. V.

The boundary condition at the still water surface (18) suggests a major difference of the semi-analytical approach from the HOS method (see, e.g., Dommermuth and Yue[36] and West et al.[37]). Equation (18) has facilitated a shift of $2k_0$ for the superharmonic wave spectrum toward the origin of the Fourier $\mathbf{k}$ space. This is a clear achievement since it permits a computational domain chosen according to the scaling of the linear wave envelope, not the smallest length of the superharmonic bound waves but the length of $2\pi/(2k_{\max} - 2k_0)$, with $k_{\max}$ ($> k_0$) the maximum wavenumber of the linear wave spectrum that can play a role. Hence, the semi-analytical approach would require less computational cost for the accurate spectral predictions of second-order superharmonic waves, as demonstrated in Sec. V A.

Eventually, the second-order superharmonic potential is obtained from

$$\Phi^{(22)}(\mathbf{x}, z, t) = \frac{1}{2}B^{(22)}(\mathbf{x}, z, t)e^{2\mathrm{i}(\mathbf{k}_0 \cdot \mathbf{x} - \omega_0 t)} \quad \text{with}$$

$$B^{(22)}(\mathbf{x}, z, t) = \int_{-\infty}^{\infty} \hat{B}^{(22)}(\mathbf{k}, z, t)\exp(\mathrm{i}\mathbf{k} \cdot \mathbf{x})d\mathbf{k},$$

(19)

which satisfies, clearly, the boundary value problem described by (15).

2. Subharmonic waves

Due to the properties of the second-order subharmonic potential $[\Phi^{(20)}]$ for the evolution of a wave group that vanishes slowly in space away from the center of the group, it is proposed to solve for $\partial_{zz}\Phi^{(20)}$ that denotes the vertical gradient of the second-order subharmonic vertical velocity instead. This can lead to the improvement of performances in numerical implementations. Introducing $w_z^{(20)} = \partial_{zz}\Phi^{(20)}$, the boundary value problem for $w_z^{(20)}$ can be derived from (12), given by

$$\nabla_3^2 w_z^{(20)} = 0 \quad \text{for } -h < z < \zeta,$$

(20a)

$$(\partial_{tt} + g\partial_z)w_z^{(20)} = -\nabla^2 F^{(20)} \quad \text{for} \quad z = 0$$

$$\partial_z w_z^{(20)} = 0 \quad \text{for} \quad z = -h.$$

(20b)

In order to avoid nonphysical homogeneous solutions in numerical implementations and also to obtain the solution for stationary waves,

the vertical gradient of the subharmonic vertical velocity $[w_z^{(20)}]$ is expressed in a form as

$$w_z^{(20)}(\mathbf{x}, z, t) = 2\mathcal{R}\left[\int\limits_{-\infty}^{\infty}\int\limits_{0}^{\infty} \hat{w}_z^{(20)}(\mathbf{k}, z, t)e^{i\mathbf{k}\cdot\mathbf{x} - i\mathbf{k}_0\cdot\mathbf{c}_{g0}t}dk_x dk_y\right] \quad (21a)$$

with

$$\hat{w}_z^{(20)}(\mathbf{k}, z, t) = \hat{w}_{z,0}^{(20)}(\mathbf{k}, t)\frac{\cosh|\mathbf{k}|(z+h)}{\cosh|\mathbf{k}|h}, \quad (21b)$$

in which $\mathcal{R}$ denotes the real component, $\mathbf{c}_{g0}$ denotes the group velocity of the carrier wave $\mathbf{k}_0$, and $\hat{w}_{z,0}^{(20)} = \hat{w}_z^{(20)}(\mathbf{k}, 0, t)$. Mathematically, the introduced factor $\exp(-i\mathbf{k}_0\cdot\mathbf{c}_{g0}t)$ denotes a radiation condition needed for stationary waves following Lighthill.[66] It is evident that the vertical gradient of the subharmonic vertical velocity, $w_z^{(20)}(\mathbf{x}, z, t)$, expressed as (21a) obeys the Laplace equation and the seabed boundary condition. The insertion of (21a) for unknown $w_z^{(20)}(\mathbf{x}, z, t)$ into the boundary condition at still water surface leads to a second-order differential equation for $\hat{w}_{z,0}^{(20)}(\mathbf{k}, t)$ as follows:

$$\left[\partial_{tt} - 2i\mathbf{k}_0\cdot\mathbf{c}_{g0} - (\mathbf{k}_0\cdot\mathbf{c}_{g0})^2 + g|\mathbf{k}|\tanh(|\mathbf{k}|h)\right]\hat{w}_{z,0}^{(20)}(\mathbf{k}, t)$$
$$= |\mathbf{k}|^2\hat{F}^{(20)}\exp(i\mathbf{k}_0\cdot\mathbf{c}_{g0}t)\ \text{ for } k_x \geq 0, \quad (22)$$

which can be readily solved for numerically with two additional initial conditions that are assumed to be known.

B. Wave elevation $\zeta^{(2)}$ at the second order

With second-order potential $\Phi^{(2)}$ given by the semi-analytical approach presented in Sec. III A, the surface elevation at the second order is obtained from [see Eq. (13.2.3) in Mei et al.,[63]]

$$\zeta^{(2)}(\mathbf{x}, t) = -\frac{1}{g}\left[\partial_t\Phi^{(2)} + \zeta^{(1)}\partial_{tz}\Phi^{(1)} + \frac{1}{2}|\nabla_3\Phi^{(1)}|^2\right]\ \text{ for } z = 0. \quad (23)$$

Inserting the envelope-type expression for the first- and second-order potentials [i.e., $\Phi^{(1)}$ and $\Phi^{(2)}$] into (23), we arrive at

$$\zeta^{(2)} = \zeta^{(20)} + (\zeta^{(22)} + \text{c.c.}), \quad (24a)$$

with

$$\zeta^{(22)} = -\frac{1}{g}\left[\frac{1}{2}(\partial_t - 2i\omega_0)B^{(22)}(\mathbf{x}, 0, t)\right.$$
$$\left. + \frac{1}{4}\left(A(\partial_t - i\omega_0)\bar{w} + \frac{1}{2}\bar{\mathbf{V}}\cdot\bar{\mathbf{V}}\right)\right]e^{2i(\mathbf{k}_0\cdot\mathbf{x} - \omega_0 t)} \quad (24b)$$

and

$$\zeta^{(20)} = -\frac{1}{g}\left[\partial_t\Phi^{(20)} + \frac{1}{4}\bar{\mathbf{V}}\cdot\bar{\mathbf{V}}^* + \frac{1}{4}(A^*(\partial_t - i\omega_0)\bar{w} + \text{c.c.})\right]$$
$$\text{for } z = 0. \quad (24c)$$

IV. TRAJECTORIES OF FLUID PARTICLES

In this section, we seek an explicit expression for the trajectories of fluid particles, which, denoted by $\mathbf{r}_p(t) = [\mathbf{x}_p(t), z_p(t)]$ with $\mathbf{x}_p$ and z_p the displacement in the horizontal plane and vertical direction, respectively, follow the definition:

$$\frac{d\mathbf{r}_p}{dt} = \mathbf{V}_p(\mathbf{r}_p(t), t), \quad (25)$$

where the subscript "p" denotes the wave parameters that follow the particle motions (i.e., in the Lagrangian framework). Equation (25) denotes an implicit equation for $\mathbf{r}_p(t)$ as it is obvious that $\mathbf{V}[\mathbf{r}_p(t), t]$ needs to be evaluated at the location [i.e., $\mathbf{r}_p(t)$] of the particles in an instant. Due to this, it is challenging to obtain an expression for particles trajectories $\mathbf{r}_p(t)$ using (25) in its present form. To resolve this, we first seek an approximate expression for the particle velocity, $\mathbf{V}_p$, in a form of power series in wave steepness and, subsequently, for particles trajectories $\mathbf{r}_p(t)$. Taylor expanding $\mathbf{V}[\mathbf{r}_p(t), t]$ about $\mathbf{r}_p = \mathbf{r}_0$ gives, to leading order,

$$\mathbf{V}_p(\mathbf{r}_p(t), t) = \mathbf{V}_p(\mathbf{r}_0, t) + \left[(\mathbf{r}_p(t) - \mathbf{r}_0)\cdot\nabla_3\right]\mathbf{V}_p|_{\mathbf{r}=\mathbf{r}_0} + \mathcal{O}(\epsilon^3), \quad (26)$$

where $\mathbf{r}_0 = (\mathbf{x}_0, z_0)$, denoting the initial position of a fluid particle, is defined as $\mathbf{r}_0 = \mathbf{r}_p(t_0)$ with an initial instant t_0, and we kept the terms up to the second order. Equation (26) suggests that the particle velocity is composed of two different velocity components; the first term on the right-hand side of the equation denotes the velocity evaluated at a fixed initial location $\mathbf{r}_0$ in the Eulerian framework, defined as $\mathbf{V}_E(\mathbf{r}_0, t) \equiv \mathbf{V}_p(\mathbf{r}_0, t)$, and the second term denotes the definition of the well-known Stokes drift velocity without averaging in the wave phase, denoted by $\mathbf{V}_{st}$. Therefore, the two different velocity components are given, to leading order, by

$$\mathbf{V}_E(\mathbf{r}_0, t) = \mathbf{V}^{(1)}(\mathbf{r}_0, t) + \mathbf{V}^{(2)}(\mathbf{r}_0, t),$$
$$\mathbf{V}_{st}(\mathbf{r}_0, t) = \left[(\mathbf{r}_p(t) - \mathbf{r}_0)\cdot\nabla_3\right]\mathbf{V}_p(\mathbf{r}_p, t)|_{\mathbf{r}_p=\mathbf{r}_0}, \quad (27)$$

where the subscript "E" denotes the Eulerian flow velocity and the subscript "st" denotes the Stokes drift, which is at least at the second order and a function of the particle trajectories. The expression for the Eulerian velocities $\mathbf{V}^{(1)}$ and $\mathbf{V}^{(2)}$ is presented in Secs. II C and III, respectively. Similarly, inserting (26) and (27) into (25) leads to the expression for the particle trajectories $\mathbf{r}_p$, to leading order, as follows:

$$\mathbf{r}_p(t) - \mathbf{r}_0 = \epsilon\Delta\mathbf{r}_p^{(1)} + \epsilon^2\Delta\mathbf{r}_p^{(2)} \quad (28a)$$

where

$$\Delta\mathbf{r}_p^{(1)} = \int_{t_0}^{t}\mathbf{V}^{(1)}(\mathbf{r}_0^{(1)}, \tau)d\tau\quad\text{and} \quad (28b)$$

$$\Delta\mathbf{r}_p^{(2)} = \int_{t_0}^{t}\left[\mathbf{V}^{(2)}(\mathbf{r}_0, \tau) + \mathbf{V}_{st}(\mathbf{r}_0, \tau)\right]d\tau, \quad (28c)$$

with $\Delta\mathbf{r}_p^{(1)}$ and $\Delta\mathbf{r}_p^{(2)}$ the net Lagrangian displacement of particles at the first order and second order, respectively. Substituting the expression for the linear velocity, i.e., $\mathbf{V}^{(1)}$ described by (10), into the expression for $\Delta\mathbf{r}^{(1)}$ described by (28b) leads to the net linear displacement of particles, $\Delta\mathbf{r}^{(1)}$, in an envelope-type form as a function of the linear wave envelope $\hat{A}(\mathbf{k}, t)$ as follows:

TABLE II. Matrix of cases examined for unidirectional wave groups. The linear waves in all cases start to propagate at $t_0 = -15T_0$ with T_0 the peak wave period; k_p and $\lambda_0 = 2\pi/k_p$ denote the wavenumber and length of the spectrum peak wave, respectively. In the table, $\epsilon = k_p A_p$ denotes the wave steepness with the peak amplitude A_p of a wave group at linear focus at the prescribed position, $x = x_f$, and time, $t = t_f$, based on (34b); h denotes constant water depth; $k_{w,1}$ and $k_{w,2}$ denote the standard deviation of an asymmetrical Gaussian (amplitude) spectrum in the lower (i.e., $k < k_p$) and upper (i.e., $k > k_p$) sideband, respectively; $\delta = \Delta k/k_p$ denotes the dimensionless bandwidth of a spectrum with Δk defined as $\Delta k = 3\max(k_{w,1}, k_{w,2})$.

Case No.	A	B	C	D	E	F	G
Spectrum	Gauss.	Jonswap	Gauss.	Gauss.	Gauss.	Gauss.	Gauss.
k_p (m^{-1})	0.0277	0.0277	0.0277	0.0277	0.0277	0.0277	0.0277
$\epsilon = k_p A_p$	0.3	0.3	0.3	0.3	0.3	0.3	0.3
x_f (m)	$-12\lambda_0$	$-12\lambda_0$	$-12\lambda_0$	$-12\lambda_0$	$-12\lambda_0$	$-12\lambda_0$	$-12\lambda_0$
t_f (s)	$-10T_0$	$-10T_0$	$-10T_0$	$-10T_0$	$-10T_0$	$-10T_0$	$-10T_0$
$k_p h$	1	1.5	1.5	1.5	1.5	2	π
$k_{w,1}$ (m^{-1})	$0.27k_p$	...	$0.27k_p$	$0.27k_p$	$0.27k_p$	$0.27k_p$	$0.27k_p$
$k_{w,2}$ (m^{-1})	$4k_{w,1}$	...	$k_{w,1}$	$4k_{w,1}$	$8k_{w,1}$	$4k_{w,1}$	$4k_{w,1}$
δ	3.24	...	0.81	3.24	6.48	3.24	3.24

$$\Delta\mathbf{r}_p^{(1)}(t) = \frac{1}{2}\begin{bmatrix}\overline{\mathbf{x}_p}(\mathbf{r}_0^{(1)}, t) \\ \overline{z_p}(\mathbf{r}_0^{(1)}, t)\end{bmatrix} e^{i(\mathbf{k}_0 \cdot \mathbf{x}_0 - \omega_0 t)} + \text{c.c. with}$$

$$\begin{bmatrix}\overline{\mathbf{x}_p} \\ \overline{z_p}\end{bmatrix} = \int_{-\infty}^{\infty}\begin{bmatrix}\hat{\mathbf{x}}_p(\mathbf{k}, z_0, t) \\ \hat{z}_p(\mathbf{k}, z_0, t)\end{bmatrix} e^{i\mathbf{k}_0 \cdot \mathbf{x}_0}d\mathbf{k}, \tag{29a}$$

and

$$\begin{bmatrix}\hat{\mathbf{x}}_p \\ \hat{z}_p\end{bmatrix} = \begin{bmatrix}\frac{i(\mathbf{k} + \mathbf{k}_0)}{|\mathbf{k} + \mathbf{k}_0|}\cosh[|\mathbf{k} + \mathbf{k}_0|(z_0 + h)] \\ \sinh|\mathbf{k} + \mathbf{k}_0|(z_0 + h)\end{bmatrix}\frac{\hat{A}(\mathbf{k}, t)}{\sinh|\mathbf{k} + \mathbf{k}_0|h}, \tag{29b}$$

where $\mathbf{x}_0$ and z_0 denote the component of $\mathbf{r}_0^{(1)}$ [i.e., $[\mathbf{x}_0, z_0] = \mathbf{r}_0^{(1)}$] in the horizontal plane and vertical direction, respectively. Equations (29a) and (29b) suggest that, if the linear envelope $\hat{A}(\mathbf{k}, t)$ is known, the net first-order Lagrangian displacement of particles can be readily obtained by using an inverse Fourier transform. With a first-order approximation to the particle trajectories ($\mathbf{r}_p$) and the velocity of particles ($\mathbf{V}_p$), the Stokes drift velocity is obtained, to the second order,

$$\mathbf{V}_{st}(\mathbf{r}_0, t) = \left[\Delta\mathbf{r}_p^{(1)} \cdot \nabla_3\right]\mathbf{V}^{(1)}(\mathbf{x}_p, t) + \mathcal{O}(\epsilon^3), \tag{30}$$

which leads to

$$\mathbf{V}_{st}(\mathbf{r}_0, t) = \mathbf{V}_{st}^{(20)} + \left[\mathbf{V}_{st}^{(22)}(\mathbf{r}_0, t) + \text{c.c.}\right], \tag{31a}$$

with

$$\mathbf{V}_{st}^{(20)}(\mathbf{r}_0, t) = \frac{1}{4}\left[\bar{\mathbf{r}}_p^* \cdot (\nabla_3 + i\mathbf{k}_0^{(3d)})\right]\bar{\mathbf{V}} + \text{c.c.} \tag{31b}$$

and

$$\mathbf{V}_{st}^{(22)}(\mathbf{r}_0, t) = \frac{1}{4}e^{2i(\mathbf{k}_0 \cdot \mathbf{x} - \omega_0 t)}\left[\bar{\mathbf{r}}_p \cdot (\nabla_3 + i\mathbf{k}_0^{(3d)})\right]\bar{\mathbf{V}}, \tag{31c}$$

where the wavenumber vector $\mathbf{k}_0^{(3d)}$ is defined as $\mathbf{k}_0^{(3d)} = [k_0, 0, 0]$ that denotes the carrier wavenumber vector in three dimensions. It is

simple to notice that the second-order Stokes drift velocities are functions of linear wave fields, suggesting that they can be easily evaluated by using a pseudospectral method[64] with given linear wave fields described in Sec. II C. With the narrowband assumption, a leading order approximation to the second-order mean Stokes drift velocity can be readily obtained from (31b) (see, e.g., Calvert *et al.*[23] and Longuet-Higgins[47]),

$$\mathbf{V}_{st}^{(20)} = \left[\frac{k_0\omega_0}{2}\frac{\cosh 2k_0(z + h)}{\sinh^2 k_0 h}|A(\mathbf{x}, t)|^2, 0, 0\right]. \tag{32}$$

The two expressions for the mean Stokes drift velocity profile, i.e., (31b) for $\mathbf{V}_{st}^{(20)}$ and (32), will be used in Sec. V B for examining the effects of wave bandwidth on the second-order mean Eulerian flow velocity and the mean Stokes drift velocity profile beneath short focused wave groups.

Inserting the second-order velocity of the Eulerian flows, i.e., $\mathbf{V}_E^{(2)} = \mathbf{V}^{(22)} + \mathbf{V}^{(20)}$, and (31a) for $\mathbf{V}_{st}^{(2)}$ into (28b) for $\Delta\mathbf{r}_p^{(2)}$ leads to the net Lagrangian displacement of particles at the second order,

$$\Delta\mathbf{r}_p^{(2)}(\mathbf{r}_0, t) = \Delta\mathbf{r}^{(20)}(\mathbf{r}_0, t) + \Delta\mathbf{r}^{(22)}(\mathbf{r}_0, t), \tag{33a}$$

with

$$\Delta\mathbf{r}_p^{(20)} = \int_{t_0}^{t}\mathbf{V}^{(20)}(\mathbf{r}_0, \tau) + \mathbf{V}_{st}^{(20)}(\mathbf{r}_0, \tau)d\tau, \tag{33b}$$
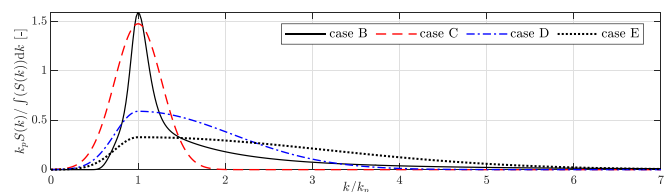
and

FIG. 1. Amplitude spectra against wavenumber for case B–E in Table II. It is worth noting that the integral of each spectrum shown in the figure is equal to k_p and the spectra for case A, D, F, and G are identical.
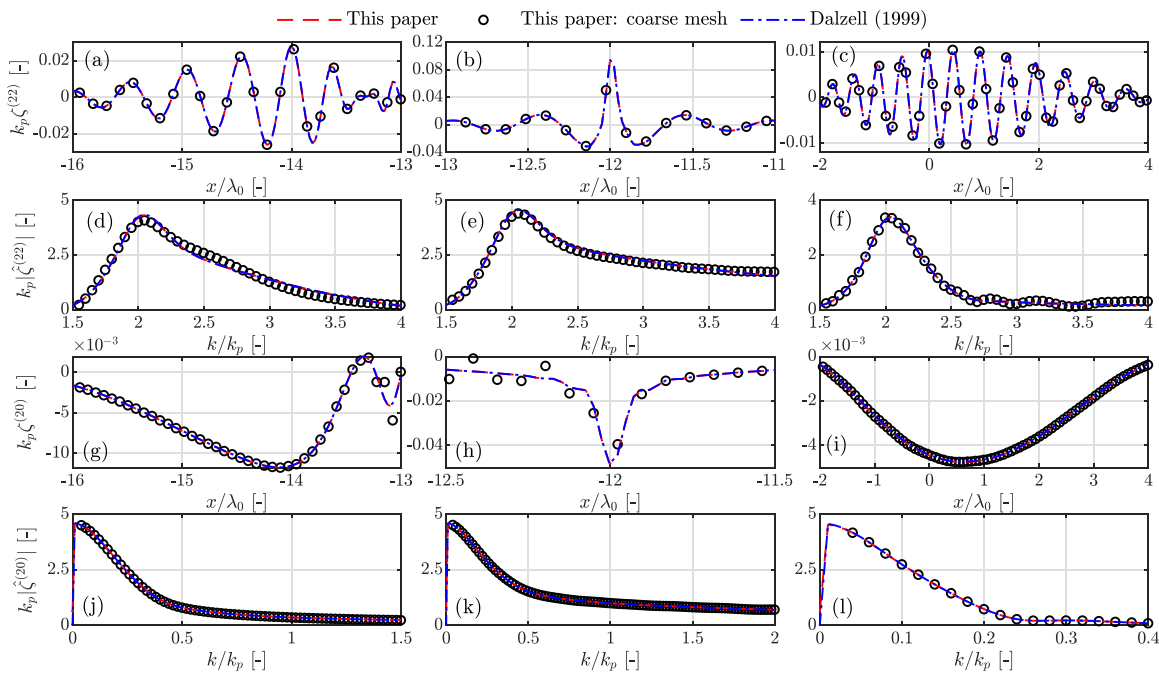
FIG. 2. Comparison of the elevation for second-order superharmonic [(a)–(f)] and subharmonic waves [(g)–(l)] at three different times between the results predicted by the semi-analytical approach from (24b) and (24c) and by Dalzell[28] in both the physical plane [(a)–(c) and (g)–(i)] and Fourier plane [(d)–(f) and (j)–(l)]. For the results based on this paper, $N_2 \approx 17$ was chosen for the finer grid (red dashed) for the second-order elevations and $N_2 = 4$ was chosen for the coarse mesh (circles) for the superharmonic elevation, where N_2 denotes the number of discrete points chosen per wavelength of the superharmonic wave. $k_p = 2\pi/\lambda_0$ denotes the spectrum peak wavenumber, where λ_0 is the spectrum peak wavelength. The linear envelope of the short wave group was obtained based on a JONSWAP spectrum, i.e., case B in Table II; Panels (a), (d), (g), and (j) $t = -14T_0$ with T_0 the period of the spectrum peak wave; (b), (e), (h), and (k) $t = -10T_0$ for the wave group at linear focus; (c), (f), (i), and (l) $t = 10T_0$.
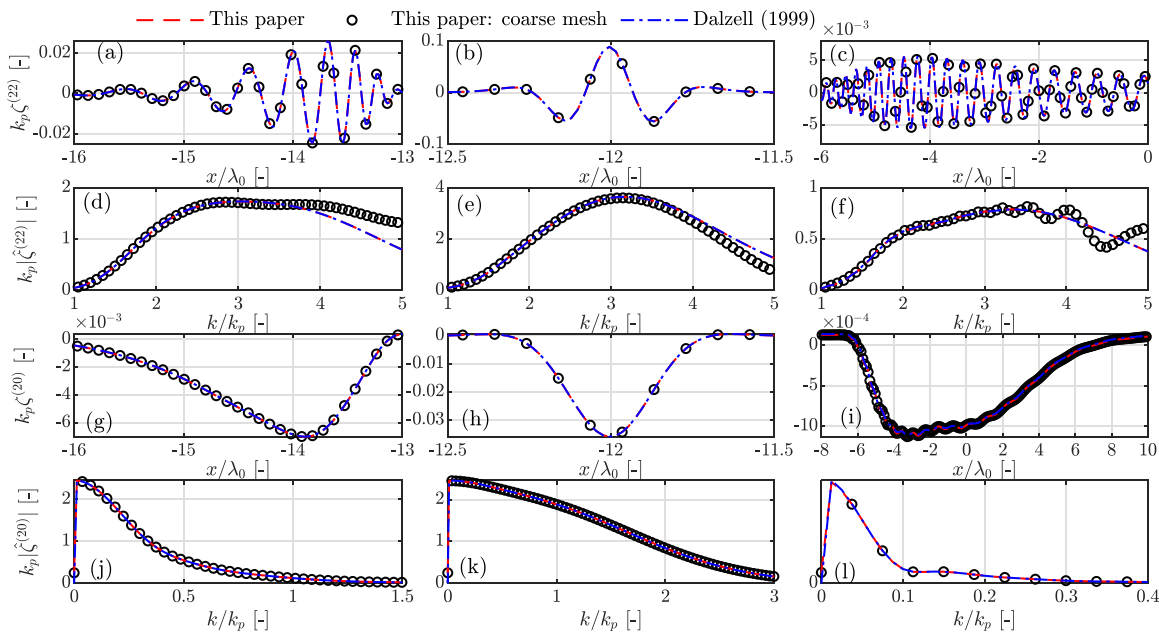

FIG. 3. For details [panels (a)–(l)], see the caption for Fig. 2 except that case D in Table II was used for this figure, instead. For the results based on this paper, $N_2 \approx 20$ was chosen for the finer grid (red dashed) and $N_2 = 5$ was chosen for the coarse mesh (circles).

$$\Delta\mathbf{r}_p^{(22)} = \int_{t_0}^{t} \mathbf{V}^{(22)}(\mathbf{r}_0, \tau) + \mathbf{V}_{st}^{(22)}(\mathbf{r}_0, \tau)d\tau + \text{c.c.,} \quad (33c)$$

where $\Delta\mathbf{r}^{(20)}$ and $\Delta\mathbf{r}^{(22)}$ denote the second-order mean and superharmonic displacement of particles measured from their initial positions, respectively. The former contributes to an overall non-zero displacement of particles in space as it does not give a zero mean in time.

V. RESULTS

In this section, we present the second-order results derived in Secs. III and IV by numerically implementing the semi-analytical approach. The approach is first validated through comparisons with Dalzell[28] in Sec. V A for the evolution of unidirectional broadband (short) focused wave groups. We examine the Stokes drift velocity profile and the trajectories of fluid particles below unidirectional short focused wave groups in Secs. V B and V C, respectively.

For the results obtained in this section, we primarily use Gaussian amplitude spectra, denoted by $S(k)$, for linear wave elevations in wavenumber. The amplitude spectra are expressed in a form as

$$S(k) = \exp\left(-\frac{(k - k_p)^2}{2k_w^2}\right) \text{ for } k > 0 \quad (34a)$$

yielding

$$\zeta^{(1)}(x, t_0) = \frac{A_p}{2}\frac{\int_0^{\infty} S(k)e^{i[k(x-x_f)-\omega(k)(t_0-t_f)]}dk}{\int_0^{\infty} S(k)dk} + \text{c.c.,} \quad (34b)$$

where k_p and k_w denote the peak wavenumber and the dimensional bandwidth of a spectrum, respectively, and A_p, x_f, and t_f denote the
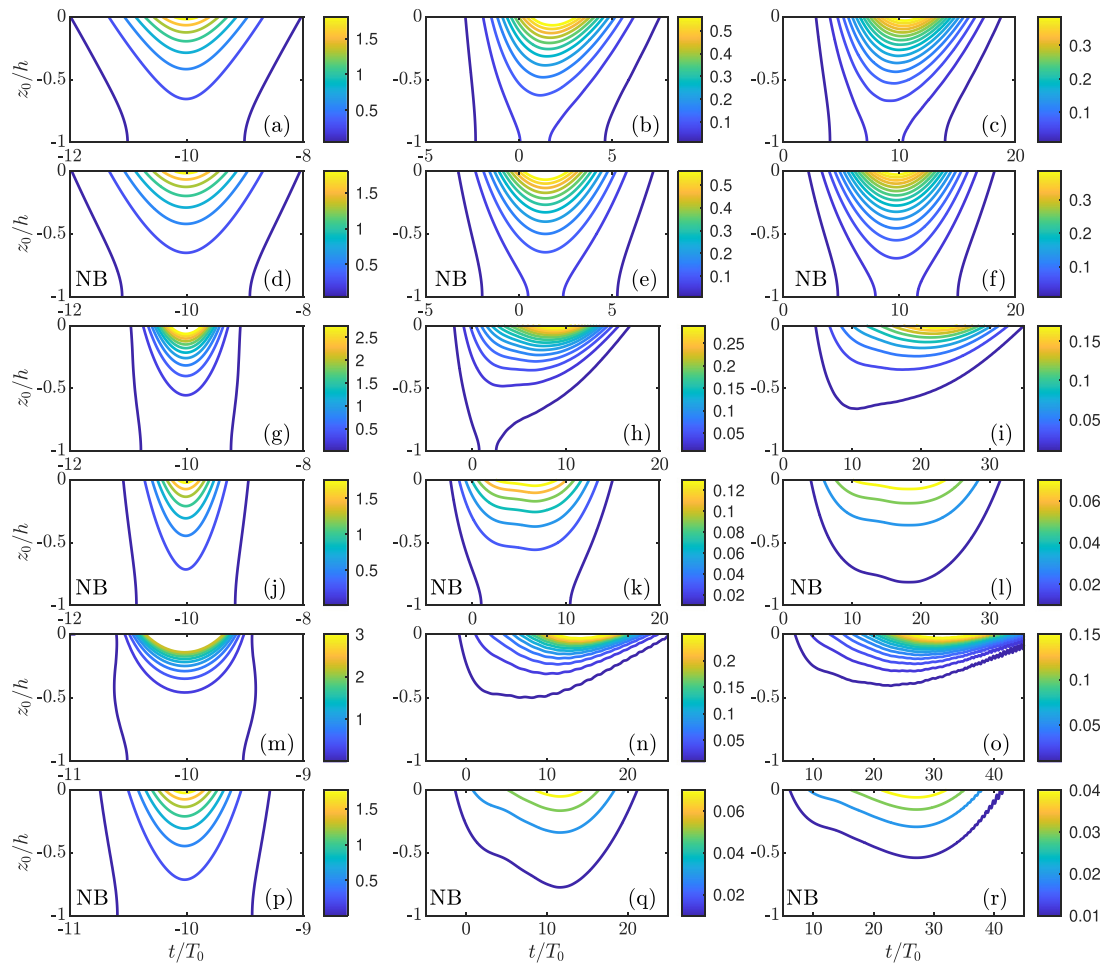

FIG. 4. Comparison of the elevation for second-order superharmonic [(a)–(f)] and subharmonic waves [(g)–(l)] at three different times between the results predicted by the semi-analytical approach from (24b) and (24c) and by Dalzell[28] in both the physical plane [(a)–(c) and (g)–(i)] and Fourier plane [(d)–(f) and (j)–(l)]. For the results based on this paper, $N_2 \approx 17$ was chosen for the finer grid (red dashed) for the second-order elevations and $N_2 = 4$ was chosen for the coarse mesh (circles) for the superharmonic elevation, where N_2 denotes the number of discrete points chosen per wavelength of the superharmonic wave, $\lambda_0/2$, where λ_0 is the spectrum peak wavelength. $k_p = 2\pi/\lambda_0$ denotes the spectrum peak wavenumber. The linear envelope of the short wave group was obtained based on a JONSWAP spectrum, i.e., case B in Table II; Panels (a), (d), (g), and (j) $t = -14T_0$ with T_0 the period of the spectrum peak wave; (b), (e), (h), and (k) $t = -10T_0$ for the wave group at linear focus; (c), (f), (i), and (l) $t = 10T_0$.

amplitude, position, and time for the group at linear focus, respectively, which are prescribed for the cases examined (see, e.g., Jonathan and Taylor[67] and Orszaghova et al.[68] for the definition of a focused wave group). In this section, asymmetrical Gaussian (amplitude) spectra are used with $k_w = k_{w,1}$ for $k < k_p$ and $k_w = k_{w,2}$ for $k \geq k_p$ where $k_{w,1}$ and $k_{w,2}$ denote the bandwidth in the lower and upper bands, respectively. A good estimate of the bandwidth for an asymmetrical Gaussian spectrum is $\delta = 3\max(k_{w,1}, k_{w,2})/k_p$ in which the factor 3 is used as it corresponds to the sidebands at which the spectrum drops by $\sim 99\%$ relative to the peak magnitude. The parameters for the cases examined in this section are shown in Table II, in which we note that the JONSWAP spectrum for case B denotes the frequency (amplitude) spectrum with the peak enhancement factor $\gamma = 3.3$.[69] The spectra for the cases in Table II are shown in Fig. 1 for illustration. Trulsen et al.[62] and Trulsen and Dysthe[70] suggest that the frameworks based on a narrowband assumption can be applicable for waves of a bandwidth in the regime $\delta \lesssim 1$. Due to this, the cases except for case C in Table II were chosen such that $\delta > 1$ for demonstrating the capability of the semi-analytical approach for broadband waves, in contrast to the narrowband frameworks.

A. Comparisons with Dalzell[28]

We validate the semi-analytical approach in this section through comparisons with the exact predictions by Dalzell.[28] For completeness, the coefficients from Dalzell[28] for the second-order elevations due to the cross interaction of two regular waves are presented in Appendix A. Comparisons of the second-order elevations between the semi-analytical approach and Dalzell[28] are shown in Figs. 2 and 3 for a JONSWAP frequency spectrum (case B) and an asymmetrical Gaussian spectrum (case D), respectively. For a fair comparison and simplicity, the inputs at the instant $t = t_0$ for the semi-analytical approach are from the exact results by Dalzell.[28]

As shown in Figs. 2 and 3, the agreement between the semi-analytical approach and Dalzell[28] is obvious for both the second-order superharmonic and subharmonic elevation. Figures 2(a), 2(g), 3(a), and 3(g) show the spatial distribution of the second-order elevations at the instant four carrier wave periods before the group at linear focus. Examining the two groups at linear focus [i.e., Figs. 2(b) and 2(h) and Figs. 3(b) and 3(h)], the JONSWAP spectrum [Figs. 2(b) and 2(h)] is about 50% larger in the peak crest for the superharmonic elevation, $\sim 30\%$ larger in the trough of the set-down, and has a shorter group length, compared to the group from the asymmetrical Gaussian spectrum [Figs. 3(b) and 3(h)]. This suggests the JONSWAP spectrum is of a larger bandwidth as expected. Figures 2(c), 2(i), 3(c), and 3(i) show the spatial distribution of the second-order elevations 20 periods after the group at linear focus, where agreement between the semi-analytical and Dalzell[28] is also clear. Comparisons for the other cases in Table II were also carried out and not shown in this section to avoid unnecessary repetitions in results. For completeness, additional comparisons for the spatial and temporal evolution of a short directional spread focused wave group are shown in Appendix B. It is demonstrated, particularly by Figs. 2 and 3, that the semi-analytical approach is capable of providing exact predictions of weakly nonlinear waves of an arbitrary bandwidth.

Introduce N_2 to denote the number of discrete points per wavelength (i.e., π/k_p) of the second-order superharmonic wave of the spectrum peak. It is known that a discrete grid in a spatial domain of a limited length would lead to the truncation of wave spectrum in the end of high wavenumbers. Due to the features of fast Fourier transform (FFT) and inverse FFT, the maximum wavenumber, denoted by k_{cut}, that can be taken into account for computations, depends on the choice of N_2 due to $k_{cut} = N_2 k_p$. In Figs. 2 and 3, the results predicted by the semi-analytical approach using a coarse mesh are also shown, where $N_2 = 4$ and $N_2 = 5$ were chosen for the evaluations of the
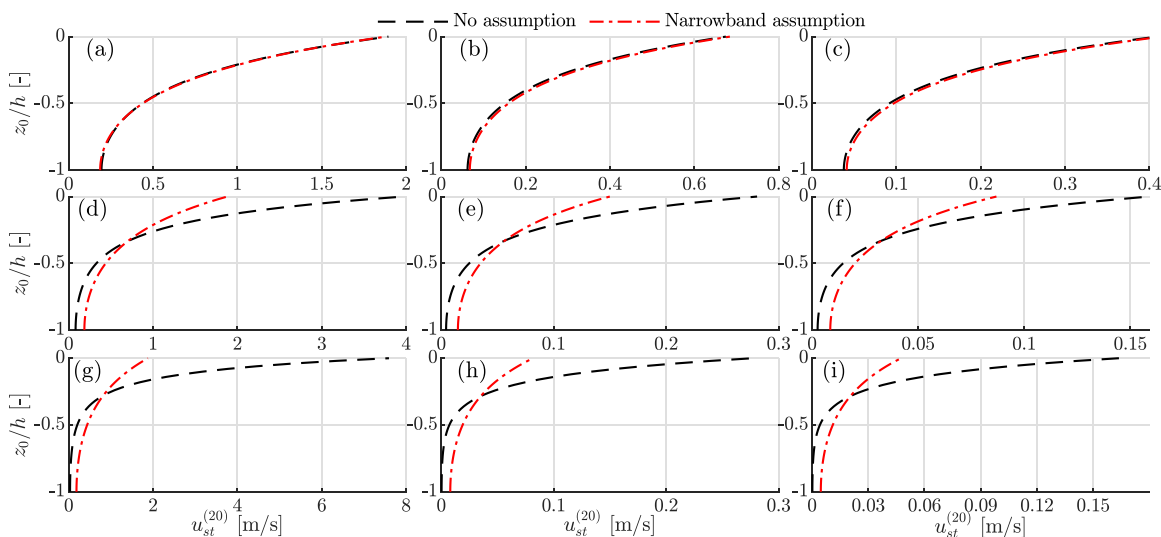

FIG. 5. Comparisons of the vertical profiles of the mean horizontal Stokes drift velocity $[u_{st}^{(20)}]$ below unidirectional focused wave groups between the results predicted by the semi-analytical approach [i.e., (31), black dashed], and by the expression (read dotted-dashed) for narrowband waves (32) for three cases with an increasing bandwidth, δ: (a)–(c) case C with $\delta = 0.81$; (d)–(f) case D with $\delta = 3.24$; (g)–(i) case E with $\delta = 6.48$; all panels predict for the time when the magnitude of A reaches the maximum, i.e., for $|A(x_0,t)| = \max(|A(x_0,t)|)$; the panels in the first column: $x_p(t_0) = x_f$ with $x_f = -12\lambda_0$ the position at linear focus, the second column: $x_p(t_0) = -5\lambda_0$, and the third column: $x_p(t_0) = 0$.

second-order superharmonic elevation. Comparing the results with these by Dalzell,[28] it is clearly seen in Figs. 2(d)–2(f) and 3(d)–3(f) that the results based on a coarse mesh can provide sufficiently accurate predictions for wavenumbers up to $k = 4k_p$, indicating the potential of the semi-analytical approach in achieving a high computational efficiency in the spectral prediction of superharmonic waves, as noted in Sec. III A 1. This advantage would be more outstanding for waves of a narrower bandwidth, which corresponds to a longer group (smaller sideband, $k_{max} - k_p$) and, hence, a smaller number of discrete points needed per wavelength. A limiting case for this is the second-order Stokes waves for which, due to $|\mathbf{k}| = 0$ in (18), the semi-analytical approach only requires a sufficiently large spatial domain such that $k_{cut} \to 0$ to provide the accurate prediction of the wave spectrum around $2k_p$.

B. Stokes drift velocity

We examine the roles of the wave bandwidth, spatiotemporal evolution, and water depth on the Stokes drift velocity beneath a short unidirectional wave group in this section. Figures 4 and 5 show the mean horizontal Stokes drift velocity predicted by using (31b) and the narrowband expression, (32), for three cases of an increasing bandwidth, δ. We proceed to the comparisons between the results by (31b)

and (32) shown in Fig. 4. Comparing Figs. 4(a)–4(c) to Figs. 4(d)–4(f) for case C with $\delta = 0.81$, differences between the broadband and narrowband predictions are minor in both the vertical structure and magnitudes, which is clearly seen in Figs. 5(a)–5(c). As the bandwidth increases, the differences become clearer, as shown in Figs. 4(g)–4(r) and 5(d)–5(i) where the predictions based on the narrowband expression show generally much weaker vertical profile shear and underestimated magnitudes of Stokes drift velocity for both case D and case E with $\delta = 3.24$ and $\delta = 6.48$, respectively. Specifically, the magnitudes of surface Stokes drift velocity from the broadband exact predictions are much larger than that predicted by the narrowband results, by a factor of 2–3, as seen in Figs. 4(h), 4(k), 4(m), 4(p), and 5(d)–5(i). Similarly, the profile shear at surface beneath the group peak shown in Figs. 5(d)–5(i) indicates an increase by a factor of ~ 3 and ~ 6 for case C and case D, respectively, based on the broadband exact predictions compared to the narrowband assumption. These suggest the need for taking into account the cross interaction of different wave components at the second order since it is neglected by the narrowband theory.

For examining the effects of the bandwidth and spatiotemporal evolution, we focus on the panels in the first, third, and fifth rows in Fig. 4, which are predicted by the semi-analytical approach. It is seen
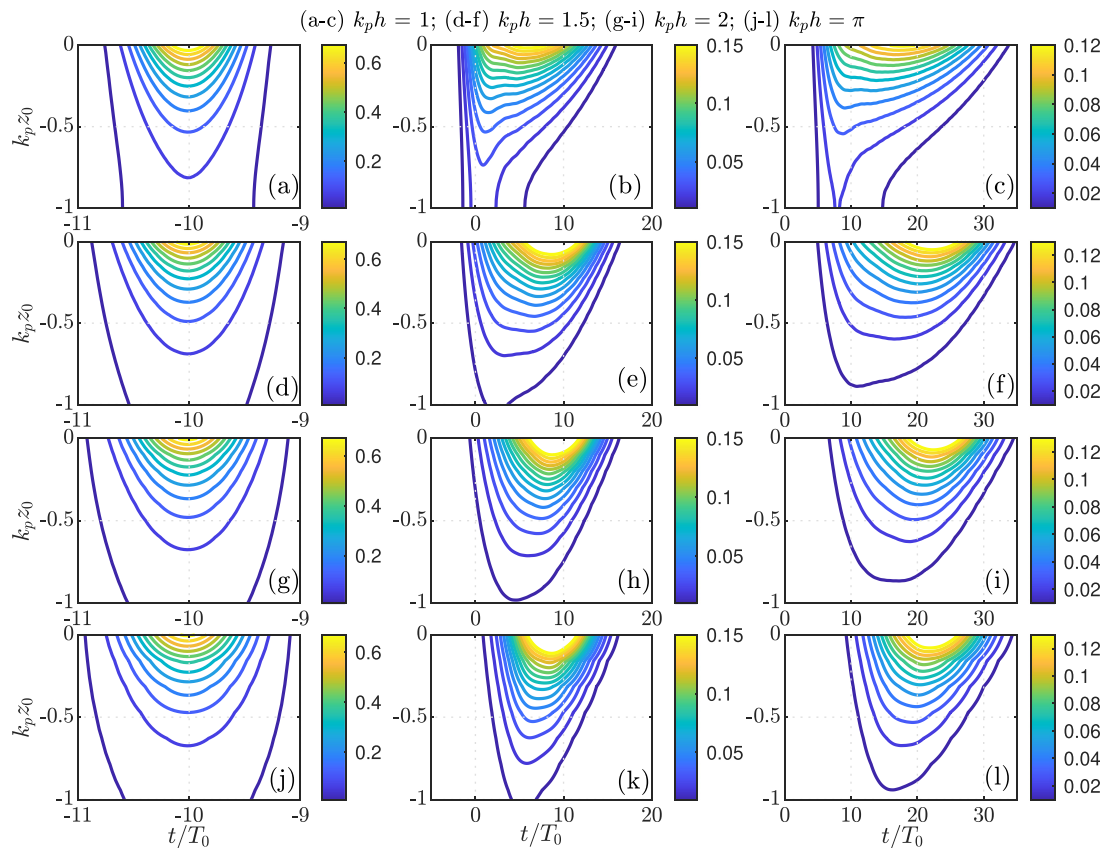

FIG. 6. The vertical-temporal distribution of the mean horizontal Stokes drift velocity below a unidirectional focused wave group predicted based on (31) by the semi-analytical approach on four different depths, k_{ph}, where k_p and h are the wavenumber of the spectrum peak wave and water depth, respectively. Panels (a)–(c) case A with $k_{ph} = 1$; (d)–(f) case D with $k_{ph} = 1.5$; (g)–(i) case F with $k_{ph} = 2$; (j)–(l) case G with $k_{ph} = \pi$. The panels in the first column for $x_p(t_0) = x_f$ with $x_f = -12\lambda_0$, the second column: $x_p(t_0) = -5\lambda_0$, and the third column: $x_p(t_0) = 0$. All contour levels are scaled by $\omega_0 |A|_{max}(x_0, t)$ with $|A|_{max} = \max[|A(x_0, t)|]$ the maximum amplitude.

that, with an increasing bandwidth, an increase and a decrease in the magnitude of Stokes drift velocity are seen at linear focus [Figs. 4(a), 4(g), and 4(m)] and post-focus times [Figs. 4(b), 4(c), 4(h), 4(i), 4(n), and 4(o)], respectively. The panels in the second and third columns, i.e., Figs. 4(b), 4(c), 4(h), 4(i), 4(n), and 4(o), show that the largest Stokes drift velocities at surface are observed at a later time for a group of a larger bandwidth, suggesting the importance of short waves in this since they generally travel slower and should be observed at a later time.

Figure 6 shows the vertical and temporal distribution of the mean Stokes drift velocity underneath a unidirectional focused wave group on four different depths, $k_p h$, varying from finite to deep water. It is clearly seen in Fig. 6 that the depth on the mean Stokes drifts plays an important role in both the vertical profile shear and the temporal distribution of the Stokes drift velocity. As the water depth ($k_p h$) increases, Figs. 6(b), 6(e), 6(h), and 6(k) show that the degree of the temporal asymmetry in the vertical profile of Stokes drift velocity tends to decrease, similar to Figs. 6(c), 6(f), 6(i), and 6(l), likely owing to linear dispersion that leads to larger discrepancies between longer and shorter waves. For the shallowest water case, Figs. 6(b) and 6(c) show that the vertical profile of the mean Stokes drift velocity observed at

earlier times [e.g., around $t/T_0 = 0$ in panel (b) and around $t/T_0 = 8$ in panel (c)] is nearly independent of water depth, indicating the features of longer waves since they propagate faster and lead to a less depth-dependent profile of Stokes drift velocity. In contrast, stronger vertical shear of Stokes drift velocity at surface is shown at later times [e.g., around $t/T_0 = 10$ in panel (b) and around $t/T_0 = 25$ in panel (c)], which indicates features of shorter waves as they propagate slower and alter more the water layer at the surface.

C. Trajectories and net mean Lagrangian displacement of particles

1. The mean particle velocities at the second order

Next we examine the mean particle velocities, below a propagating wave group, that determine the non-zero net displacement of particles. As derived in Sec. IV, the mean particle velocities comprise of two components: the Eulerian flows, $\mathbf{V}^{(20)}(\mathbf{x}_0, z_0, t)$, measured at a fixed initial position, and the mean Stokes drift velocity, $\mathbf{V}_{st}^{(20)}$, due to the linear displacement and linear velocity of the particles. We take a look at the two
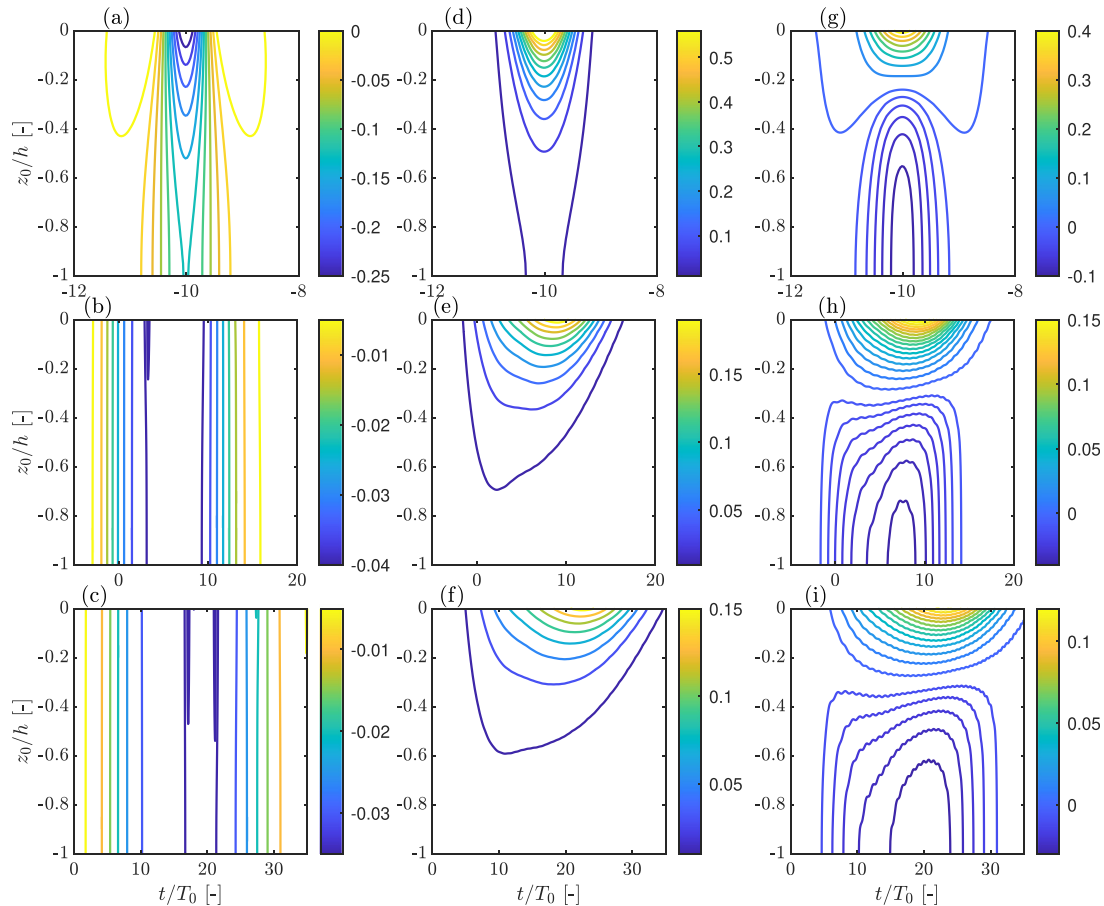

FIG. 7. Vertical structure of second-order mean Eulerian return flows (a)–(c), mean Stokes drift velocity (d)–(f), and the leading-order mean particle velocities (g)–(i) in the form of the sum of the two varying in time (t/T_0) underneath a short unidirectional focused wave group for particles at three different initial locations; (a), (d), and (g) $x_p(t_0) = x_f$ with $x_f = -12\lambda_0$ and (b), (e), and (h) $x_p(t_0) = -5\lambda_0$, and (c), (f), and (i) $x_p(t_0) = 0$. All contour levels are scaled by $\omega_0 |A|_{max}(x_0, t)$ with $|A|_{max} = \max[|A(x_0, t)|]$ the maximum amplitude. Case D in Table II ($\delta = 3.24$) was used for computations.

different components in Fig. 7. Figure 7 shows the spatiotemporal evolution of the vertical structure of the mean horizontal Eulerian flows [Figs. 7(a)–7(c)], mean Stokes drift velocities [Figs. 7(d)–7(f)], and the summation of the two that denotes the mean particle velocity [Figs. 7(g)–7(i)] underneath a unidirectional broadband focused wave group. As seen in Figs. 7(a)–7(c) and as expected, the mean horizontal Eulerian velocity appears as return flows since it has a negative sign and propagates in the opposing direction to the main propagation direction of the group. Comparing the position at linear focus [Fig. 7(a)] with the other two positions [Figs. 7(b) and 7(c)], the Eulerian velocity is more dependent on z_0 and has generally a larger magnitude.

In contrast, the mean Stokes drift velocity [Figs. 7(d)–7(f)] holds a positive sign throughout the water column and decreases quickly with depth (i.e., the profile has a strong shear near the surface). Figures 7(d)–7(f) show that the magnitude and vertical structure of the Stokes drift velocity vary with the initial particle positions, x_0. Due to the different signs and vertical structures of the Stokes drift and Eulerian

return flows, Figs. 7(g)–7(i) show that the mean velocity of the particles is positive in a layer near the water surface, whereas it is negative in a layer near the seabed. Therefore, there exists a depth $z_0 = -h_t$, with the depth h_t at which the mean particle velocity is zero. The magnitude, temporal evolution, and vertical structures of the particle velocities vary at different initial positions x_0, which determine the key features of the net displacement of particles examined in Sec. V C 2.

2. Particle trajectories and displacements below focused wave groups

Figure 8 shows the trajectories of particles [panels (a)–(d), (f)–(j), and (l)–(o)] beneath a short wave group starting from rest at different depths, z_0, and initial horizontal positions, x_0, and the net mean displacements [panels (e), (k), and (p)] of these particles after the group has passed. Examining the vertical profile of the trajectories initially at a position x_0, we see from Figs. 8(a)–8(d) that the particles near surface, i.e., Figs. 8(a) and 8(b), and at depths, i.e., Figs. 8(c) and 8(d),
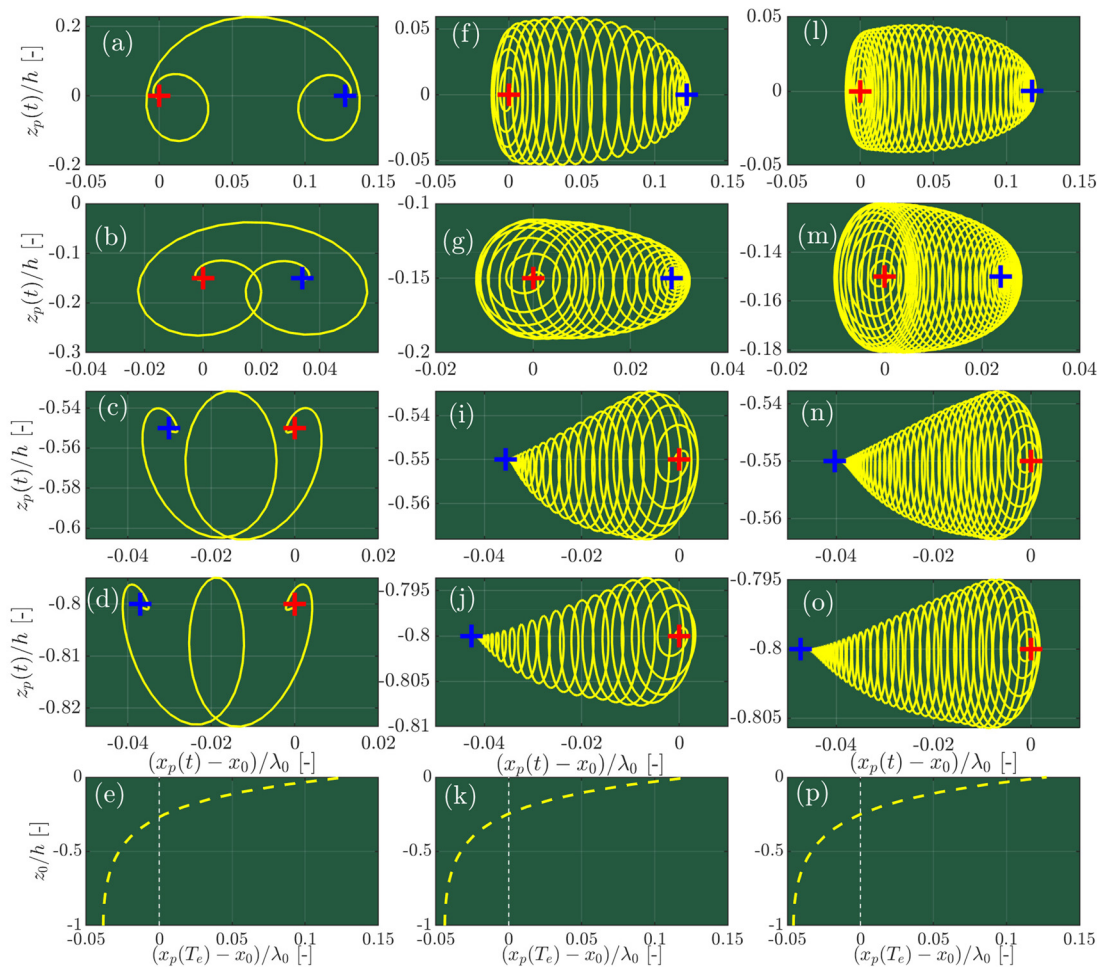

FIG. 8. Particle trajectories [(a)–(d), (f)–(j), and (l)–(o)] underneath a short unidirectional focused wave group and the net mean horizontal displacement of particles at different depths (z_0); Panels (a)–(e) $x_p(t_0) = x_f$ with $x_f = -12\lambda_0$; (f)–(k) $x_p(t_0) = -5\lambda_0$, and (l)–(p) $x_p(t_0) = 0$. This figure used case D for computations. All particles start to propagate at rest, indicated by marker "+" in red before the wave group arrives, and they stop moving after the group has passed, indicated by marker "+" in blue.

show a positive and negative net mean horizontal displacement, respectively, as also seen in Fig. 8(e). The trajectories of the particles near surface are shown to be of a larger magnitude in the oscillating motion. For the particles starting downstream the position at linear focus, shown in Figs. 8(f)–8(j), more rounds of oscillations at a smaller magnitude in motion can be observed as the group passes, which is more so for the particles further downstream shown in Figs. 8(l)–8(o). Comparing the panels (e), (k), and (p) in Fig. 8, no clear differences are shown in the vertical structure as well as magnitudes in the net mean horizontal displacements evaluated at the three different initial horizontal positions. This is surprising as the corresponding particle velocities in Figs. 7(g)–7(i) have demonstrated clear differences in both magnitude and vertical-temporal distributions for particles at different positions, based on which one would expect, as a result, differences in the vertical structures of the net mean horizontal velocities. The unchanged vertical profile in the net mean horizontal displacements of

particles below a group may be understood from that the developed wave fields are within a conserved and stationary system that would lead to conserved kinetic energy due to particle motions in space.

Next we examine the effects of the wave bandwidth and depth on the trajectories and the net mean horizontal displacements of particles, as shown in Figs. 9 and 10 where cases of an increasing bandwidth and depth are chosen, respectively, with the other parameters remaining the same for all the cases. Focusing on the particle trajectories, it is seen in Fig. 9 that an increased bandwidth leads to opposing effects on the oscillating motions of particles starting at a position at linear focus and downstream; an enhanced (decreased) magnitude but reduced (increased) periods in the oscillating motions are observed for the surface particles starting at linear focus (downstream). We remark that the total horizontal mass transport is not assumed zero, different from that in Longuet-Higgins[47] [i.e., Eqs. (2)–(4) therein]. This explains the obvious nonzero integral for the net mean horizontal displacements
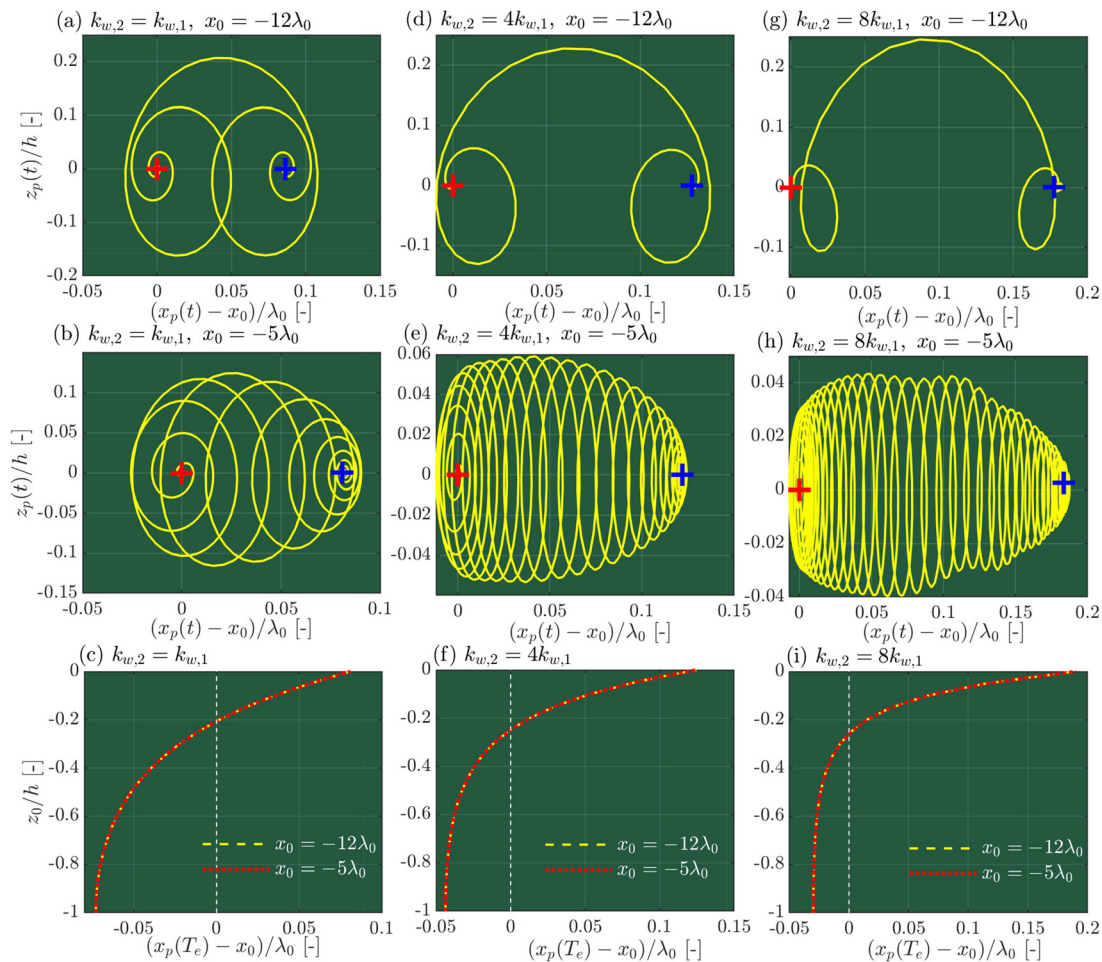

FIG. 9. Particle trajectories (panels in the top and middle row) underneath short unidirectional focused wave groups and the net mean horizontal displacement [panels (c), (f), and (i)] of the particles at different depths (z_0); the panels in the top row: $x_p(t_0) = x_f$ with $x_f = -12\lambda_0$, the second row: $x_p(t_0) = -5\lambda_0$. Panels (a)–(c) were calculated based on case C; (d)–(f): case D; (g)–(i): case E. All particles start to propagate at rest, indicated by marker "+" in red before the wave group arrives and they stop to move after the group has passed, indicated by marker "+" in blue.

over the water column shown in Figs. 9(c), 9(f), and 9(i). As a result, this would lead to a constant shift of the net mean horizontal displacements of all particles throughout the water column, which does not affect the observation in Figs. 9(c), 9(f), and 9(i) that an increased bandwidth leads to larger differences between the net displacements of the particles at still water surface and at seabed, indicating that the bandwidth of waves on a finite depth plays an important role in both particle velocities and mean horizontal displacements at different depths.

The trajectories of the surface particles in the first and second columns in Fig. 10 indicate that the depth leads to negligible effects in the oscillating magnitudes and periods in the motion of the surface particles. In contrast, it is clearly shown in Figs. 10(c), 10(f), 10(j), and 10 (m) that, as water depth (i.e., $k_p h$ increases, the particles near water surface experience an increased net mean horizontal displacement relative to the particles at seabed.

VI. CONCLUSIONS

In this paper, a semi-analytical approach has been proposed for the description of weakly nonlinear multi-directional surface waves. Based on a Stokes and harmonic expansion, an envelope-type framework for second-order wave fields in wave steepness has been derived and the approach proposes solving for the wave fields by using a pseudospectral method and a numerical scheme for the superharmonic and subharmonic wave fields at still water surface. The approach permits computational operations of order $N\ln(N)$ due to the pseudospectral method, where N denotes the total number of the discrete points in space chosen according to the scaling of the envelope of linear wave elevation. This suggests that N can be chosen of a much smaller value than some other numerical methods, such as the High-Order Spectral method (see, e.g., Dommermuth and Yue[36] and West *et al.*[37]). Comparisons between the results predicted by the
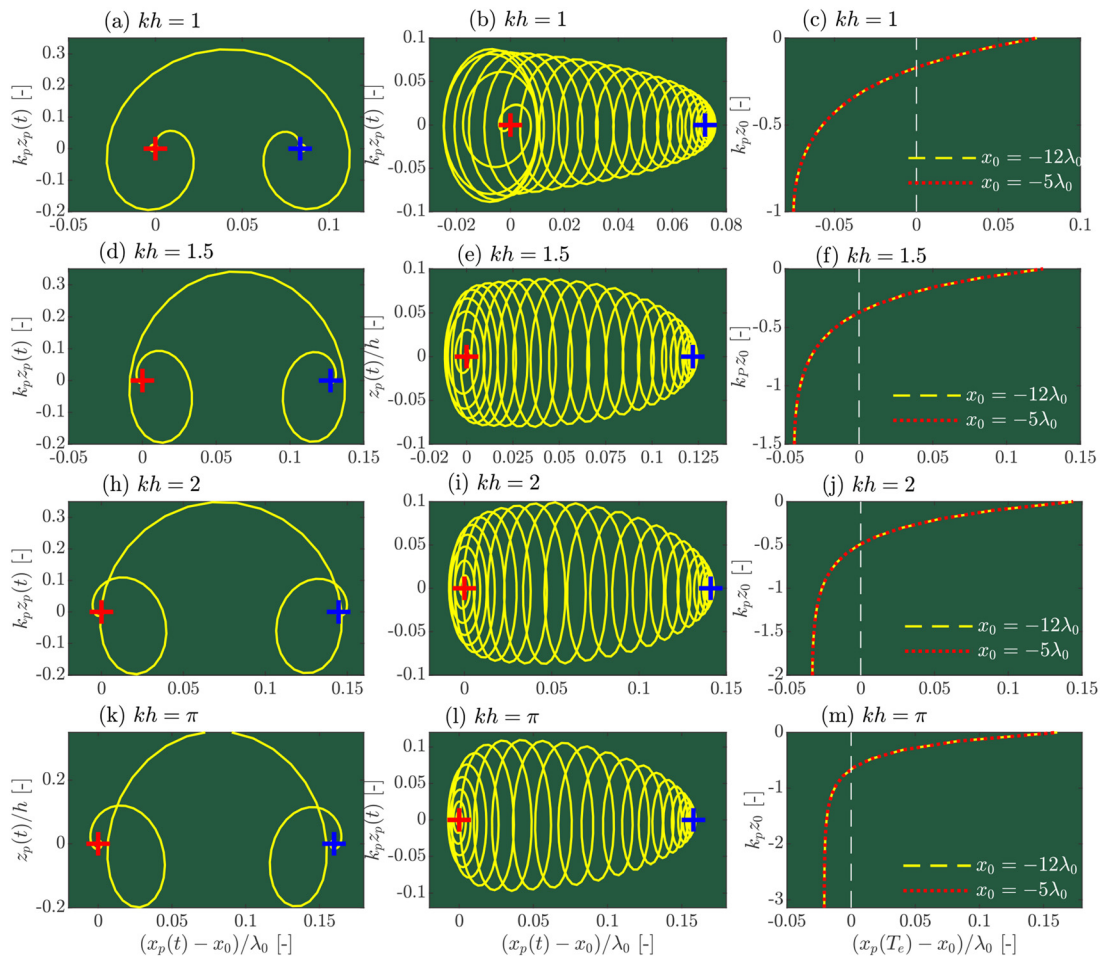

FIG. 10. Surface particles trajectories (panels in the left and middle column) underneath short unidirectional focused wave groups and the net mean horizontal displacements [panels (c), (f), (j), and (m)] of the particles at different depths (z_0); the panels in the left column: $x_p(t_0) = x_f$ with $x_f = -12\lambda_0$, the middle column: $x_p(t_0) = -5\lambda_0$. Panels (a)–(c) were calculated based on case A with $k_{ph} = 1$ where k_p and h denote the wavenumber of a spectrum peak wave and water depth, respectively; (d)–(f): case D with $k_{ph} = 1.5$; (h) and (i): case F with $k_{ph} = 2$; (k)–(m): case G with $k_{ph} = \pi$. All particles start to propagate at rest, indicated by marker "+" in red before the wave group arrives and they stop moving after the group has passed, indicated by marker "+" in blue.

semi-analytical approach and the exact results by Dalzell[28] are presented for the evolution of focused wave groups generated from broadband asymmetrical Gaussian and JONSWAP spectrum. It has been demonstrated that the semi-analytical approach can provide exact results as that by Dalzell[28] and that four or five discrete points per wavelength of the second-order superharmonic peak wave can provide sufficiently accurate spectral predictions of superharmonic waves for wavenumbers up to four times the peak wavenumber for truly broadband wave spectra. This approach allows for general extensions for the description of fully nonlinear waves as well as for the interaction of waves with ambient environments, e.g., subsurface currents, turbulence, and varying seabed. These aspects will be addressed in future work.

Based on the semi-analytical approach, an envelope-type framework for the trajectories of particles up to the second order in wave steepness has also been derived in this paper. The effects of wave bandwidth, water depth, and the spatiotemporal evolution of unidirectional wave groups on the particle trajectories, net mean horizontal displacements of particles, and Stokes drift velocities underneath broadband unidirectional focused wave groups have been examined. It is found that the spatiotemporal evolution of a wave group plays an important role in the linear trajectories of particles and the vertical profiles and magnitudes of the Stokes drift velocity. It has negligible effects on the vertical (depth) structure of the net mean horizontal displacement of particles. In contrast, an increased bandwidth and depth can lead to an increased mean horizontal displacement of particles at the surface relative to the particles at the seabed. Comparing the results obtained from a narrowband assumption with these by the semi-analytical approach, this paper has shown that the narrowband assumption leads to large discrepancies in the estimates of the second-order mean Eulerian return flow and the velocity profile of Stokes drift beneath wave groups of dimensionless bandwidth larger than 1, i.e., for $\Delta k/k_p > 1$ with the side bandwidth in wavenumber Δk and the spectrum peak wavenumber k_p, confirming the applicability regime of narrowband theory suggested by Trulsen et al.[62]

ACKNOWLEDGMENTS

APPENDIX A: COEFFICIENTS FOR THE SECOND-ORDER WAVE ELEVATIONS[28]

Based on Dalzell,[28] the second-order superharmonic and subharmonic wave elevation can be given by
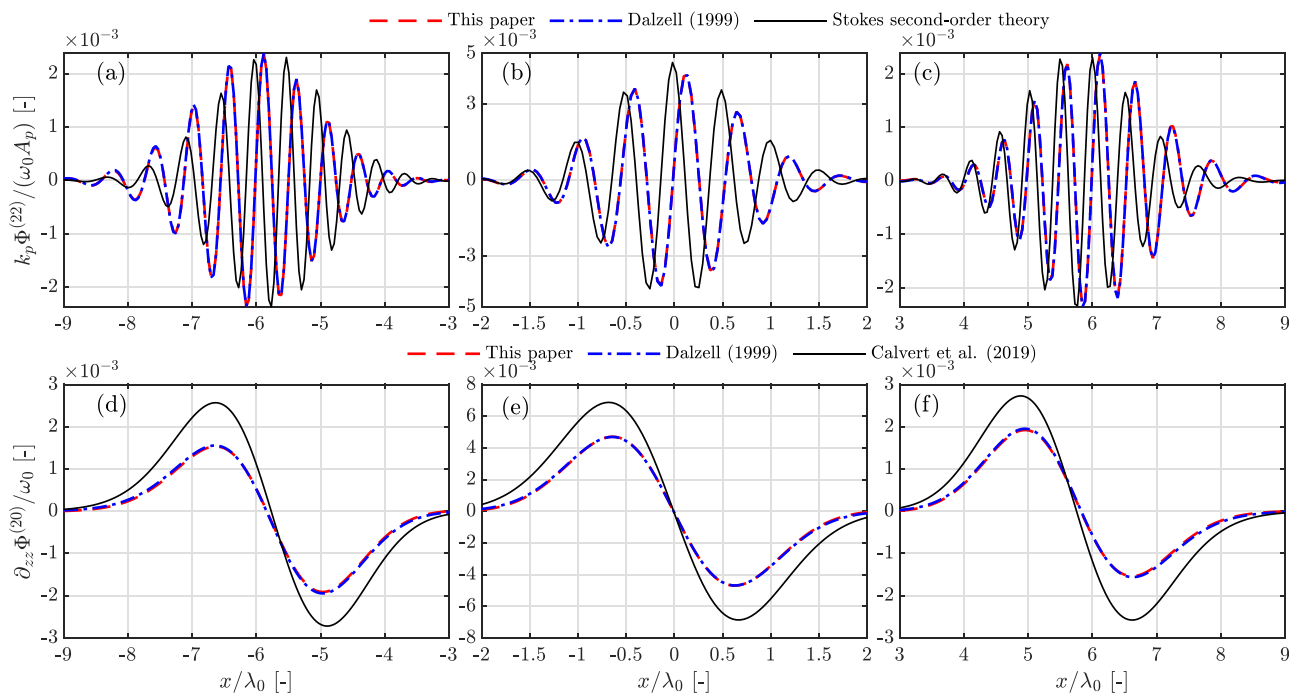

FIG. 11. Comparison of the second-order superharmonic potential $\Phi^{(22)}$ [panels (a)–(c)] between the results predicted by the semi-analytical approach, by Dalzell[28] (exact), and Stokes second-order theory (cf. Davey and Stewartson[20]) and comparison of $w_z^{(20)}$ [panels (d)–(f)] between the results predicted by the semi-analytical approach, by Dalzell[28] (exact), and by Calvert et al.[23] that is based on a narrowband assumption. All panels show the results at still water surface and follow the center of the group for $y = 0$. The linear envelope of the short wave group was obtained based on a symmetrical directional spread Gaussian spectrum, where $k_p = 0.027\,69$ m^{-1} is the peak wavenumber, $k_{w,1} = k_{w,2} = 0.0046$ m^{-1} is the bandwidth in wavenumber, $\theta_0 = 0°$, $\theta_w = 10°$, $x_f = 0 \times \lambda_0$, and $t_f = 0 \times T_0$, where λ_0 and T_0 denotes the wavelength and period of the spectrum peak wave. The group starts to propagate at $t = -15T_0$. Panels (a) and (d) $t = -10T_0$; (b) and (e) $t = 0 \times T_0$ for the wave group at linear focus; (c) and (f) $t = 10T_0$.
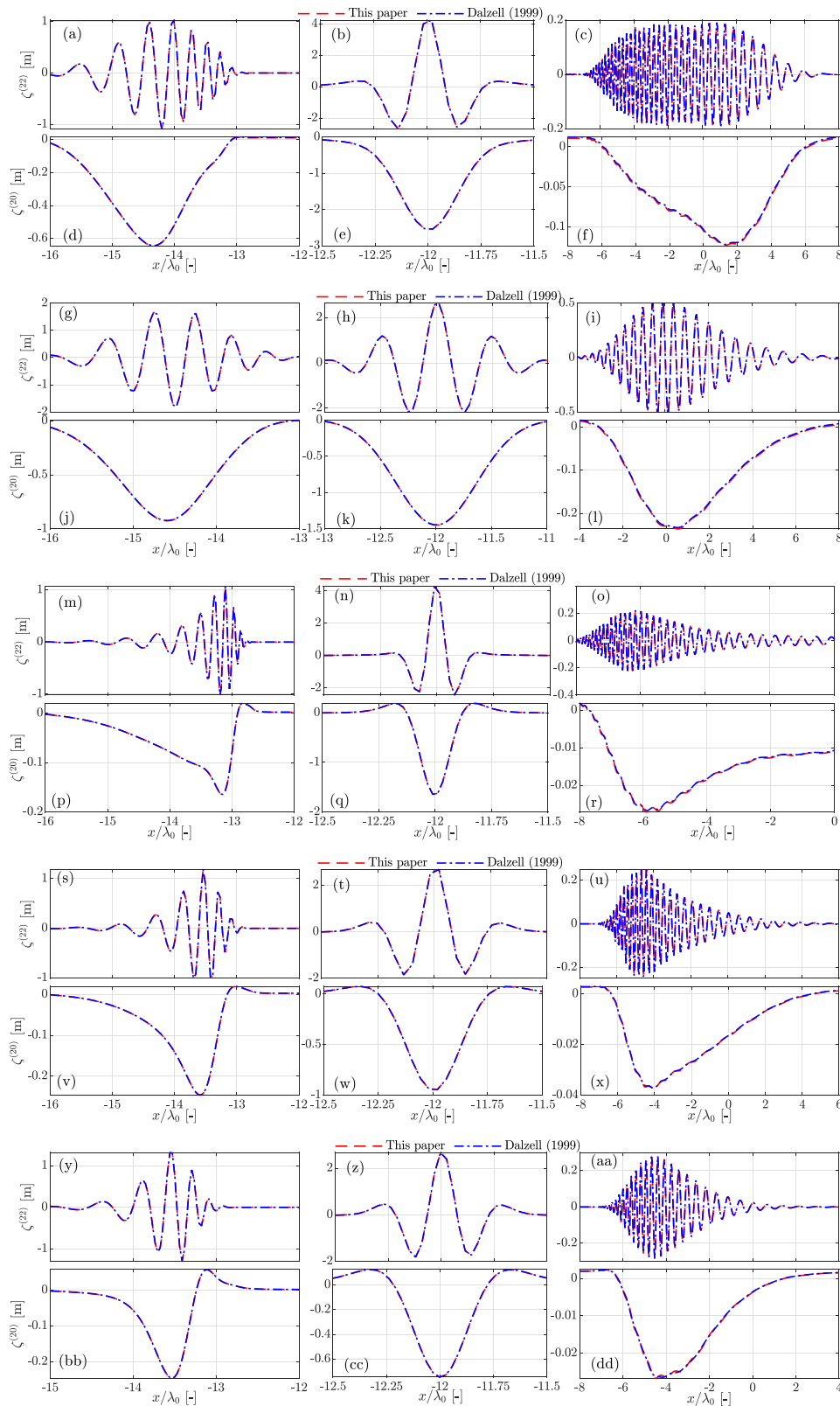
FIG. 12. Comparisons of second-order elevations for case A (a)–(f), case C (g)–(l), case E (m)–(r), case F (s)–(x), and case G (y)–(dd). Other parameters are the same as Fig. 2.

$$\zeta^{(22)}(\mathbf{x},t) = \sum_{i=0}^{N}\sum_{|\mathbf{k}_j|\geq|\mathbf{k}_i|}^{j=N} \frac{|\hat{\zeta}_i||\hat{\zeta}_j|}{2}\left[\frac{\omega_i^2+\omega_j^2}{2}\right.$$

$$-\frac{\omega_i\omega_j}{2g}\left(1-\frac{\cos(\mu_i-\mu_j)}{\tanh(|\mathbf{k}_i|h)\tanh(|\mathbf{k}_j|h)}\right)\frac{Q_+(\mathbf{k}_i,\mathbf{k}_j,\omega_i,\omega_j)}{D_+(\mathbf{k}_i,\mathbf{k}_j,\omega_i,\omega_j)}$$

$$\left.+\frac{\omega_i+\omega_j}{2gD_+}\left(\frac{\omega_i^3}{\sinh^2(|\mathbf{k}_i|h)}+\frac{\omega_j^3}{\sinh^2(|\mathbf{k}_j|h)}\right)\right]\cos(\psi_j+\psi_i),$$

$$(A1a)$$

$$\zeta^{(20)}(\mathbf{x},t) = \sum_{i=0}^{N}\sum_{|\mathbf{k}_j|\geq|\mathbf{k}_i|}^{j=N} \frac{|\hat{\zeta}_i||\hat{\zeta}_j|}{2}\left[\frac{\omega_i^2+\omega_j^2}{2}\right.$$

$$+\frac{\omega_i\omega_j}{2g}\left(1+\frac{\cos(\mu_i-\mu_j)}{\tanh(|\mathbf{k}_i|h)\tanh(|\mathbf{k}_j|h)}\right)\frac{Q_-(\mathbf{k}_i,\mathbf{k}_j,\omega_i,\omega_j)}{D_-(\mathbf{k}_i,\mathbf{k}_j,\omega_i,\omega_j)}$$

$$\left.+\frac{\omega_i-\omega_j}{2gD_-}\left(\frac{\omega_i^3}{\sinh^2(|\mathbf{k}_i|h)}-\frac{\omega_j^3}{\sinh^2(|\mathbf{k}_j|h)}\right)\right]\cos(\psi_i-\psi_j),$$

$$(A1b)$$

where $\psi_i(\mathbf{x},t) = \mathbf{k}_i\cdot\mathbf{x}-\omega_i t+\theta_i$ and $\psi_j(\mathbf{x},t) = \mathbf{k}_j\cdot\mathbf{x}-\omega_j t+\theta_j$ denote the wave phase functions, where $\omega_i = \omega(|\mathbf{k}_i|)$ and $\omega_j = \omega(|\mathbf{k}_j|)$ are the angular frequencies of linear free waves, θ_i and θ_j are the initial free wave phases; μ_i and μ_j denote the direction of wave vector $\mathbf{k}_i$ and $\mathbf{k}_j$, respectively; and $|\hat{\zeta}_i|$ and $|\hat{\zeta}_j|$ denote the amplitude of linear free wave $\mathbf{k}_i$ and $\mathbf{k}_j$, respectively,

$$D_\pm = (\omega_i\pm\omega_j)^2 - g|\mathbf{k}_i\pm\mathbf{k}_j|\tanh(|\mathbf{k}_i\pm\mathbf{k}_j|h), \qquad (A2a)$$

and

$$Q_\pm = (\omega_i\pm\omega_j)^2 + g|\mathbf{k}_i\pm\mathbf{k}_j|\tanh(|\mathbf{k}_i\pm\mathbf{k}_j|h). \qquad (A2b)$$

APPENDIX B: ADDITIONAL RESULTS

In this section, additional results for the evolution of a multi-directional wave group are examined. The angular distribution of the linear wave group is expressed as a Gaussian distribution

$$\Xi(\mu) = \exp\left(-\frac{(\mu-\mu_0)^2}{2\mu_w^2}\right), \qquad (B1)$$

where μ_0 and μ_w denote the propagation direction of the spectrum peak wave and the directional width, respectively. Together with the amplitude spectrum presented in Sec. V A, the linear elevation is given by

$$\zeta^{(1)}(\mathbf{x},t) = \frac{A_p}{2S_\Sigma\Xi_\Sigma}\sum_{n=1}^{N}\sum_{m=1}^{M}S(|\mathbf{k}_{n,m}|)\Xi(\mu_m)e^{i(\mathbf{k}_{n,m}\cdot(\mathbf{x}-\mathbf{x}_f)-\omega(|\mathbf{k}_{n,m}|)(t_0-t_f))}$$

$$(B2a)$$

with

$$S_\Sigma = \sum_{n=1}^{N}S(|\mathbf{k}_{n,m}|) \quad\text{and}\quad \Xi_\Sigma = \sum_{m=1}^{M}S(\mu_m), \qquad (B2b)$$

where $\mathbf{k}_{n,m} = [|\mathbf{k}_n|\cos(\mu_m),|\mathbf{k}_n|\sin(\mu_m)]$ denotes the wave vector of a free wave and $|\mathbf{k}_n|$ and μ_m denote evenly spaced discrete points in wavenumber and directions, respectively.

Figure 11 shows the comparison of the evolution of a directional spread focused wave group between the predictions by the semi-analytical approaches, by Dalzell,[28] and narrowband approximations (i.e., the Stokes second-order theory and Calvert et al.[23]). Good agreement between the semi-analytical approach and Dalzell[28] is clear, whereas the differences between the approximate results and the other two exact methods can be clearly seen.

Figure 12 shows the comparison of second-order wave elevations between the predictions by the semi-analytical approach and by Dalzell[28] for the evolution of two dimensional focused wave groups through input based on case A, C, E, F, and G in Table II, where good agreement between the semi-analytical approach and Dalzell[28] has been confirmed, in addition to Figs. 2 and 3.

DATA AVAILABILITY

The data that support the findings of this study and the numerical functions that implement the semi-analytical approach are available from the corresponding author upon reasonable request.

REFERENCES

[1] M. W. Dingemans, *Water Wave Propagation Over Uneven Bottoms* (World Scientific, 1997), Vol. 13.

[2] A. Slunyaev, M. Klein, and G. F. Clauss, "Laboratory and numerical study of intense envelope solitons of water waves: Generation, reflection from a wall, and collisions," Phys. Fluids **29**, 047103 (2017).

[3] Y. Li, Y. Zheng, Z. Lin, T. A. A. Adcock, and T. S. van den Bremer, "Surface wavepackets subject to an abrupt depth change. Part I: Second-order theory," J. Fluid Mech. **915**, A72 (2021).

[4] M. Derakhti and J. T. Kirby, "Breaking-onset, energy and momentum flux in unsteady focused wave packets," J. Fluid Mech. **790**, 553 (2016).

[5] X. Barthelemy, M. Banner, W. Peirson, F. Fedele, M. Allis, and F. Dias, "On a unified breaking onset threshold for gravity waves in deep and intermediate depth water," J. Fluid Mech. **841**, 463–488 (2018).

[6] J. Zhang and M. Benoit, "Wave–bottom interaction and extreme wave statistics due to shoaling and de-shoaling of irregular long-crested wave trains over steep seabed changes," J. Fluid Mech. **912**, A28 (2021).

[7] K. Trulsen, A. Raustøl, S. Jorde, and L. Rye, "Extreme wave statistics of long-crested irregular waves over a shoal," J. Fluid Mech. **882**, R2 (2020).

[8] Y. Zheng, Z. Lin, Y. Li, T. Adcock, Y. Li, and T. van den Bremer, "Fully nonlinear simulations of extreme waves provoked by strong depth transitions: The effect of slope," Phys. Rev. Fluids **5**, 064804 (2020).

[9] Y. Li, S. Draycott, Y. Zheng, Z. Lin, T. Adcock, and T. van den Bremer, "Why do rogue waves occur atop abrupt depth transitions," J. Fluid Mech. **919**, R5 (2021).

[10] C. Lawrence, K. Trulsen, and O. Gramstad, "Statistical properties of wave kinematics in long-crested irregular waves propagating over non-uniform bathymetry," Phys. Fluids **33**, 046601 (2021).

[11] G. Ducrozet, A. Slunyaev, and Y. Stepanyants, "Transformation of envelope solitons on a bottom step," Phys. Fluids **33**, 066606 (2021).

[12] G. B. Whitham, *Linear and Nonlinear Waves* (John Wiley & Sons, 1974), Vol. 42.

[13] R. G. Dean and R. A. Dalrymple, *Water Wave Mechanics for Engineers and Scientists* (World Scientific Publishing Company, 1991), Vol. 2.

[14] O. M. Phillips, "On the dynamics of unsteady gravity waves of finite amplitude. Part 1. The elementary interactions," J. Fluid Mech. **9**, 193–217 (1960).

[15] M. S. Longuet-Higgins, "Resonant interactions between two trains of gravity waves," J. Fluid Mech. **12**, 321–332 (1962).

[16] J. N. Newman, *Marine Hydrodynamics* (The MIT Press, 1977).

[17] B. Molin, "Second-order diffraction loads upon three-dimensional bodies," Appl. Ocean Res. **1**, 197–202 (1979).

[18]J. Grue, "On four highly nonlinear phenomena in wave theory and marine hydrodynamics," Appl. Ocean Res. **24**, 261–274 (2002).

[19]K. B. Dysthe, "Note on a modification to the nonlinear Schrödinger equation for application to deep water waves," Proc. R. Soc. London, Ser. A **369**, 105–114 (1979).

[20]A. Davey and K. Stewartson, "On three-dimensional packets of surface waves," Proc. R. Soc. London, Ser. A **338**, 101–110 (1974).

[21]K. Trulsen, O. T. Gudmestad, and M. G. Velarde, "The nonlinear Schrödinger method for water wave kinematics on finite depth," Wave Motion **33**, 379–395 (2001).

[22]O. Gramstad, "The Zakharov equation with separate mean flow and mean surface," J. Fluid Mech. **740**, 254 (2014).

[23]R. Calvert, C. Whittaker, A. Raby, P. H. Taylor, A. G. L. Borthwick, and T. S. van den Bremer, "Laboratory study of the wave-induced mean flow and set-down in unidirectional surface gravity wave packets on finite water depth," Phys. Rev. Fluids **4**, 114801 (2019).

[24]U. Brinch-Nielsen and I. G. Jonsson, "Fourth order evolution equations and stability analysis for Stokes waves on arbitrary water depth," Wave Motion **8**, 455–472 (1986).

[25]A. V. Slunyaev, "A high-order nonlinear envelope equation for gravity waves in finite-depth water," J. Exp. Theor. Phys. **101**, 926–941 (2005).

[26]K. Hasselmann, "On the non-linear energy transfer in a gravity-wave spectrum," J. Fluid Mech. **12**, 481–500 (1962).

[27]J. N. Sharma and R. G. Dean, "Second-order directional seas and associated wave forces," Soc. Pet. Eng. J. **21**, 129–140 (1981).

[28]J. F. Dalzell, "A note on finite depth second-order wave–wave interactions," Appl. Ocean Res. **21**, 105–111 (1999).

[29]G. G. Stokes, "On the theory of oscillatory waves," Trans. Cambridge Philos. Soc. **8**, 441–455 (1847).

[30]G. Wei, J. T. Kirby, S. T. Grilli, and R. Subramanya, "A fully nonlinear Boussinesq model for surface waves. Part 1. Highly nonlinear unsteady waves," J. Fluid Mech. **294**, 71–92 (1995).

[31]G. Z. Forristall, "Wave crest distributions: Observations and second-order theory," J. Phys. Oceanogr. **30**, 1931–1943 (2000).

[32]V. H. Chu and C. C. Mei, "On slowly-varying Stokes waves," J. Fluid Mech. **41**, 873–887 (1970).

[33]V. H. Chu and C. C. Mei, "The non-linear evolution of Stokes waves in deep water," J. Fluid Mech. **47**, 337–351 (1971).

[34]A. Armaroli, D. Eeltink, M. Brunetti, and J. Kasparian, "Nonlinear stage of Benjamin–Feir instability in forced/damped deep-water waves," Phys. Fluids **30**, 017102 (2018).

[35]K. Dysthe, H. E. Krogstad, and P. Müller, "Oceanic rogue waves," Annu. Rev. Fluid Mech. **40**, 287–310 (2008).

[36]D. G. Dommermuth and D. K. P. Yue, "A high-order spectral method for the study of nonlinear gravity waves," J. Fluid Mech. **184**, 267–288 (1987).

[37]B. J. West, K. A. Brueckner, R. S. Janda, D. M. Milder, and R. L. Milton, "A new numerical method for surface hydrodynamics," J. Geophys. Res.: Oceans **92**, 11803–11824, https://doi.org/10.1029/JC092iC11p11803 (1987).

[38]E. Lo and C. C. Mei, "A numerical study of water-wave modulation based on a higher-order nonlinear Schrödinger equation," J. Fluid Mech. **150**, 395–416 (1985).

[39]M. A. Tayfun, "Narrow-band nonlinear sea waves," J. Geophys. Res., C: Oceans Atmos. **85**, 1548–1552, https://doi.org/10.1029/JC085iC03p01548 (1980).

[40]M. A. Tayfun, "On narrow-band representation of ocean waves: 1. Theory," J. Geophys. Res., C: Oceans Atmos. **91**, 7743–7752, https://doi.org/10.1029/JC091iC06p07743 (1986).

[41]M. A. Tayfun and M. A. Alkhalidi, "Distribution of sea-surface elevations in intermediate and shallow water depths," Coastal Eng. **157**, 103651 (2020).

[42]T. Tang and T. Adcock, "The influence of finite depth on the evolution of extreme wave statistics in numerical wave tanks," Coastal Eng. **166**, 103870 (2021).

[43]D. Myrhaug, "Some statistical aspects of wave-induced drift in sea states," Coastal Eng. **78**, 53–56 (2013).

[44]D. Myrhaug, H. Wang, and L. E. Holmedal, "Stokes drift estimation for deep water waves based on short-term variation of wave conditions," Coastal Eng. **88**, 27–32 (2014).

[45]A. P. Engsig-Karup, H. B. Bingham, and O. Lindberg, "An efficient flexible-order model for 3D nonlinear water waves," J. Comput. Phys. **228**, 2100–2118 (2009).

[46]H. Bihs, W. Wang, T. Martin, and A. Kamath, "REEF3D: FNPF–A flexible fully nonlinear potential flow solver," in Proceedings of International Conference on Offshore Mechanics and Arctic Engineering (2020).

[47]M. S. Longuet-Higgins, "Mass transport in water waves," Philos. Trans. R. Soc., A **245**, 535–581 (1953).

[48]A. D. D. Craik and S. Leibovich, "A rational model for Langmuir circulations," J. Fluid Mech. **73**, 401–426 (1976).

[49]J. C. McWilliams, J. M. Restrepo, and E. M. Lane, "An asymptotic theory for the interaction of waves and currents in coastal waters," J. Fluid Mech. **511**, 135 (2004).

[50]T. S. van den Bremer and ∅. Breivik, "Stokes drift," Philos. Trans. R. Soc., A **376**, 20170104 (2018).

[51]∅. Breivik, P. A. E. M. Janssen, and J.-B. Bidlot, "Approximate Stokes drift profiles in deep water," J. Phys. Oceanogr. **44**, 2433–2445 (2014).

[52]∅. Breivik and K. H. Christensen, "A combined Stokes drift profile under swell and wind sea," J. Phys. Oceanogr. **50**, 2819–2833 (2020).

[53]A. Webb and B. Fox-Kemper, "Impacts of wave spreading and multidirectional waves on estimating stokes drift," Ocean Modell. **96**, 49–64 (2015).

[54]J. Grue and J. Kolaas, "Experimental particle paths and drift velocity in steep waves at finite water depth," J. Fluid Mech. **810**, 1–10 (2017).

[55]J. Grue and A. Jensen, "Orbital velocity and breaking in steep random gravity waves," J. Geophys. Res.: Oceans **117**, 7013, https://doi.org/10.1029/2012JC008024 (2012).

[56]M. McIntyre, "On the 'wave momentum' myth," J. Fluid Mech. **106**, 331–347 (1981).

[57]T. S. van den Bremer and P. H. Taylor, "Estimates of Lagrangian transport by surface gravity wave groups: The effects of finite depth and directionality," J. Geophys. Res.: Oceans **120**, 2701–2722, https://doi.org/10.1002/2015JC010712 (2015).

[58]T. van den Bremer, C. Whittaker, R. Calvert, A. Raby, and P. Taylor, "Experimental study of particle trajectories below deep-water surface gravity wave groups," J. Fluid Mech. **879**, 168 (2019).

[59]H. A. Schäffer, "Second-order wavemaker theory for irregular waves," Ocean Eng. **23**, 47–88 (1996).

[60]M. Paprota, "Experimental study on spatial variation of mass transport induced by surface waves generated in a finite-depth laboratory flume," J. Phys. Oceanogr. **50**, 3501–3511 (2020).

[61]Y. Li, S. Draycott, T. A. A. Adcock, and T. S. van den Bremer, "Surface wave-packets subject to an abrupt depth change. Part II: Experimental analysis," J. Fluid Mech. **915**, A72 (2021).

[62]K. Trulsen, I. Kliakhandler, K. B. Dysthe, and M. G. Velarde, "On weakly non-linear modulation of waves on deep water," Phys. Fluids **12**, 2432–2437 (2000).

[63]C. C. Mei, M. Stiassnie, and D. K. P. Yue, *Theory and Applications of Ocean Surface Waves: Nonlinear Aspects* (World Scientific, 2005), Vol. 23.

[64]B. Fornberg and G. B. Whitham, "A numerical and theoretical study of certain nonlinear wave phenomena," Philos. Trans. R. Soc., A **289**, 373–404 (1978).

[65]F. Bonnefoy, D. Le Touzé, and P. Ferrant, "A fully-spectral 3D time-domain model for second-order simulation of wavetank experiments. Part A: Formulation, implementation and numerical properties," Appl. Ocean Res. **28**, 33–43 (2006).

[66]M. Lighthill, "Contributions to the theory of waves in non-linear dispersive systems," IMA J. Appl. Math. **1**, 269–306 (1965).

[67]P. Jonathan and P. H. Taylor, "On irregular, nonlinear waves in a spread sea," J. Offshore Mech. Arct. Eng. **119**, 37–41 (1997).

[68]J. Orszaghova, P. H. Taylor, A. Borthwick, and A. Raby, "Importance of second-order wave generation for focused wave group run-up and overtopping," Coastal Eng. **94**, 63–79 (2014).

[69]K. Hasselmann *et al.*, "Measurements of wind-wave growth and swell decay during the joint north sea wave project (JONSWAP)," Report No. 12, 1973.

[70]K. Trulsen and K. B. Dysthe, "A modified nonlinear Schrödinger equation for broader bandwidth gravity waves on deep water," Wave Motion **24**, 281–289 (1996).